

Machine-learned cloud classes from satellite data for process-oriented climate model evaluation

Arndt Kaps, Axel Lauer, Gustau Camps-Valls, *Fellow, IEEE*, Pierre Gentine, Luis Gómez-Chova, *Senior Member, IEEE*, Veronika Eyring .

Abstract—Clouds play a key role in regulating climate change but are difficult to simulate within Earth system models (ESMs). Improving the representation of clouds is one of the key tasks towards more robust climate change projections. This study introduces a new machine-learning based evaluation method relying on satellite observations to improve understanding of the representation of clouds and their relevant processes in models. The proposed method is capable of assigning distributions of established cloud types to coarse data. It facilitates a more objective evaluation of clouds in ESMs and improves the consistency of cloud process analysis. The method is built on satellite data from the MODIS instrument labelled by deep neural networks with cloud types as defined by the World Meteorological Organization (WMO), using cloud type labels from CloudSat as ground truth. The method is applicable to datasets with information about physical cloud variables comparable to MODIS satellite data and at sufficiently high temporal resolution. We apply the method to alternative satellite data from the Cloud_cci project (ESA Climate Change Initiative), coarse grained to typical resolutions of climate models. The resulting cloud type distributions are physically consistent and the horizontal resolutions typical of ESMs are sufficient to apply our method. We recommend outputting crucial variables required by our method for future ESM data evaluation. This will enable the use of labelled satellite data for a more systematic evaluation of clouds in climate models.

Index Terms—clouds, climate modelling, CloudSat, MODIS, CUMULO dataset, ESA Cloud_cci, machine learning, process-oriented model evaluation

A. Kaps (arndt.kaps@dlr.de), A. Lauer and V. Eyring with the Deutsches Zentrum für Luft- und Raumfahrt (DLR), Institut für Physik der Atmosphäre, Oberpfaffenhofen, Germany

G. Camps-Valls and L. Gómez-Chova with Image Processing Laboratory (IPL), University of Valencia, Valencia, Spain

P. Gentine with Department of Earth and Environmental Engineering, Columbia University, NY, USA and Center for Learning the Earth with Artificial Intelligence and Physics (LEAP), Columbia University, NY, USA

V. Eyring with University of Bremen, Institute of Environmental Physics (IUP), Bremen, Germany

Funding for this study was provided by the European Research Council (ERC) Synergy Grant “Understanding and Modelling the Earth System with Machine Learning (USMILE)” under the Horizon 2020 research and innovation programme (Grant agreement No. 855187). Gentine acknowledges support from National Science Foundation Science and Technology Center for Learning the Earth with Artificial Intelligence and Physics (LEAP) L.G.C. and G.C.V. work is partially funded by the Spanish Ministry of Science and Innovation (project PID2019-109026RB-I00). The work was supported by the ESA Climate Change Initiative Climate Model User Group (ESA CCI CMUG). This work used resources of the Deutsches Klimarechenzentrum (DKRZ) granted by its Scientific Steering Committee (WLA) under project ID bd1179. The authors gratefully acknowledge the Leibniz Supercomputing Centre for funding this project by providing computing time on its Linux-Cluster. We thank Valentina Zantedeschi, Fabrizio Falasca and their co-authors for kindly providing the CUMULO dataset and code

I. INTRODUCTION

Earth system models (ESMs, also referred to as climate models) are important tools not only to improve our understanding of present-day climate but also to project climate change under different plausible future scenarios. For this, climate models have been continuously improved and extended over the last decades from relatively simple atmosphere-only models to complex state-of-the-art ESMs including many processes such as the biogeochemical cycle, e.g. those participating in the latest (sixth) phase of the Coupled Model Intercomparison Project (CMIP6, [1]). This increasing complexity of models is needed to represent key feedbacks that affect climate change, but also requires innovative and comprehensive model evaluation and analysis approaches to assess the performance of these models [2], given the increase in the number of tunable parameters in the models. In particular, the simulation of clouds and their interactions with the climate system remain major challenges for ESMs [3]. As a consequence, cloud feedback mechanisms such as the shortwave radiative effect of low clouds, which are critical for long-term climate projections, have proven to be hard to quantify confidently [4]–[6]. Furthermore, the representation of clouds has been identified as one of the primary sources of inter-model spread in state-of-the-art ESMs [7]. An improved representation of cloud processes is therefore an essential component in addressing these issues [8]–[10]. Any new changes in the models, e.g. by a more detailed representation of the underlying physics, need to be assessed thoroughly. The most common method to assess the performance of the models is to compare the statistical properties of clouds, such as the climatological mean and variability of important physical quantities, to observations. This approach has led to significant improvements in the performance of climate models in several aspects over the last generations of climate models contributing to CMIP [11].

Observations are usually obtained from long-term satellite products providing near-global coverage, which have proven to be well suited for the evaluation of climate models [e.g. 12]. However, such conventional satellite products have some known limitations. Depending on the satellite product, these limitations include: varying spatial and temporal coverage over the globe, difficulty in resolving vertical features with passive instruments, and biases induced by the retrieval algorithms as the underlying inversion problem is typically under-determined [e.g. 13]. Because of those specific instrument characteristics such as detection limits and orbital parameters of the satellite itself, including overpass times and viewing geometry, the model output is typically not directly comparable to the

satellite retrievals. One approach to address this is to use satellite simulators, which convert the climate model output to a product that is more closely comparable with the specific satellite product [14]. Such simulators, however, are not always readily available for all model experiments and also cannot solve all of these issues. Consequently, the efficiency and accuracy of climate model evaluation can still be improved, which is why new approaches to the aforementioned issues are being developed. For example, evaluation software such as the Earth System Model Evaluation Tool (ESMValTool, [15]–[18]) address some of these issues by providing standardized metrics and diagnostics, therefore making scientific analysis more comparable.

The method we present here is a new approach to ESM evaluation, designed to facilitate process-oriented evaluation of clouds in climate models and to address some of the apparent limitations of using conventional observational data. We use *a priori* knowledge about the characteristics of different cloud classes based on the cloud type classification of the World Meteorological Organization (WMO). This way cloud processes can be highlighted in further evaluation by exploiting this *a priori* knowledge. Our approach extends the recent development of machine learning based cloud classification methods for satellite data [19]–[23] to climate models. Machine learning based cloud classification is not a new idea [e.g. 24], but has only recently become feasible for large-scale application due to the increase in available computing power. An important distinction between classification methods is whether they are supervised or unsupervised. The former relies on previously assigned classes and the latter aims at automatically finding distinct new classes. Supervised classification relies on the assumption that the assigned classes fit the purpose, whereas the user has limited control over the makeup of the classes in unsupervised methods. Therefore, supervised methods allow for interpreting the final results without additional analysis steps but require a set of labelled data [20], [23]. If the goal is to find classes that are as distinct as possible, or if no previously labelled data are available, unsupervised methods are preferable [21], [22].

Labelled datasets allow for a more detailed and more direct interpretation of cloud classes in the respective satellite data in contrast to comparatively coarse classifications as used for example in the D-Series of the International Cloud Climatology Project (ISCCP, [25]). To our knowledge, no high-resolution ($O(1 \text{ km})$) cloud-class-labelled satellite data have been used for analysis and evaluation of ESMs, so far. In a recent study, a convolutional neural network was used on $(4000 \text{ km})^2$ grid cells to assign the amount of each of four cloud classes per cell [26]. In [26], the classes are derived from WMO classes detected from surface observations and the method is applicable to climate model output. Previous studies have used clustering for satellite products and the output of satellite simulators from models for unsupervised classification of clouds [10], [27], [28]. In these studies, morphological cloud regimes are then assigned to the identified clusters, according to the average physical properties of each cluster. Such a classification offers valuable insights into how individual models represent clouds in a more specific way than simple climatologies of physical variables would. However, in addition to being built on the

rather low resolution of $(280 \text{ km})^2$ of the ISCCP-D1 [25] product, uncertainties and artifacts introduced by the satellite simulators can affect the results [29]. Other studies have classified satellite data by cloud regime to investigate specific cloud properties such as radiative effects or precipitation [30], [31]. Recently, clustering methods for cloud regimes have been applied to current-generation climate models using the $1^\circ \times 1^\circ$ resolution ISCCP-H product [32] for training, which has a much higher resolution than ISCCP-D1 [33]. Most of the clusters found this way are labeled with cloud regimes named after cloud types defined by the WMO.

Our method aims at establishing this connection between observations and models without the requirement to assign cloud classes *a posteriori*. This is achieved by using high-resolution satellite products (MODIS, CloudSat) and subsequent machine learning. We propose a multi-stage machine learning framework trained on satellite data to relate cloud-relevant atmospheric properties of any model grid cell to a distribution of WMO cloud classes. The first stage uses deep learning to expand cloud class labels extracted from the CloudSat 2B-CLDCLASS-LIDAR dataset [34], which has sparse coverage, to the MODIS dataset, which has extensive coverage across the globe. The network is trained using physical variable retrievals from the MODIS cloud product [35] as features. The second stage translates this to lower resolutions ($O(10 - 100 \text{ km})$) more comparable to climate models, using a Random Forest algorithm to learn a mapping from physical variables to cloud type distributions. This allows us to assign a cloud class distribution to coarse grid cells. Statistical analysis can be conducted on these distributions in the same manner as for the traditionally used physical variables, but in the phase space of cloud classes.

Performing analysis in this cloud class space has several advantages. Firstly, a layer of subjective interpretation is removed by directly presenting the results in terms of cloud classes clearly defined by the underlying classification algorithm (CloudSat, [34]). Because we are using well-known pre-defined classes, the resulting cloud class distributions can then be analysed and interpreted in a process-based manner as the key processes driving formation and evolution differ between the WMO cloud classes. Thus, a selection of physical properties related to cloud processes for further interpretation is not required. Secondly, as the underlying deep learning algorithm learns from high resolution 3-dimensional data, the models are implicitly analysed in a horizontally super-resolved manner which also takes into account information about the vertical structure of clouds, i.e. learning from a combination of 2-dim and 3-dim data can potentially expose information from the vertical that would not be included in the cloud top view.

The paper is outlined as follows. In section II, we describe the satellite products we used and introduce the two machine learning methods applied in this proof-of-concept. In section III, we use our results to establish (1) that a neural network can be used to accurately assign cloud class labels to satellite data, (2) that this labelled satellite data provides a sufficient basis to train a regression model relating physical variable retrievals from satellites to cloud class distributions in coarse grid cells and (3) that application to a coarse grained version

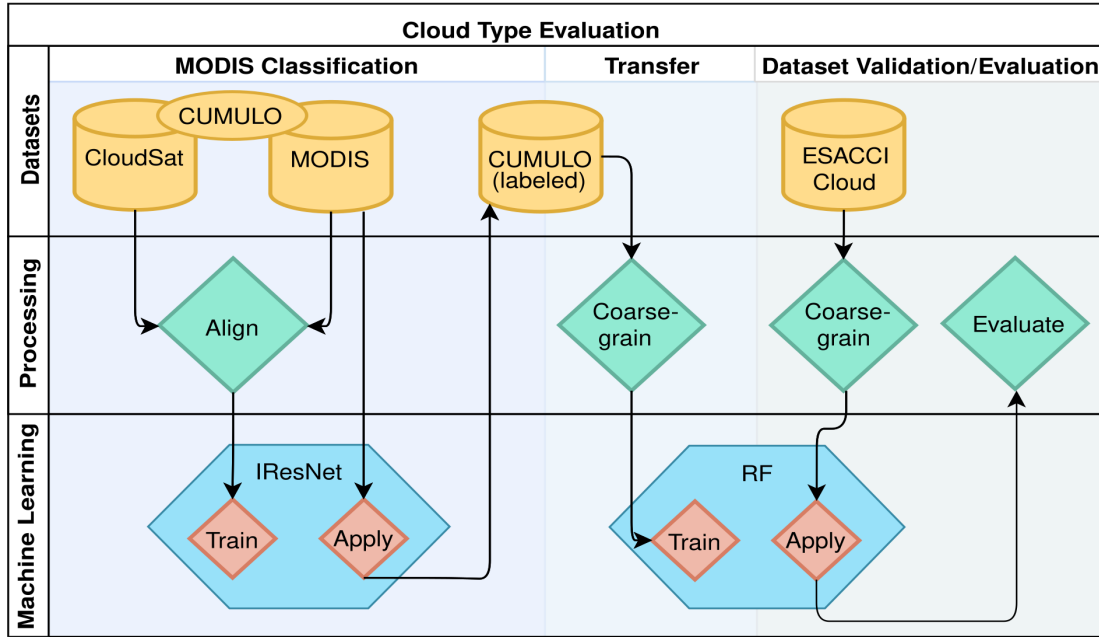


Fig. 1: Workflow schematic of the three blocks containing two machine learning stages (lowest row) with subsequent evaluation: (1) The IResNet is trained on the CUMULO dataset containing MODIS data aligned with CloudSat labels, and then applied on the unlabeled full-swath MODIS images at 1 km resolution, yielding the fully labelled CUMULO dataset. (2) This data is then coarse grained to better match ESM resolutions (~ 100 km) and used to train a random forest (RF) regression model to provide cloud class distributions. (3) The RF is applied to unseen data, allowing validation performance or evaluation of the target dataset.

of the alternative ESA Cloud_cci satellite product [36] is possible, showing the potential of the framework. A discussion and an outlook is presented in section IV, highlighting certain input variables and temporal and spatial resolutions required to apply this framework to ESM output in the future.

II. METHODS

A. Overview

The proposed framework to evaluate clouds in climate models is using data from the Moderate Resolution Imaging Spectroradiometer (MODIS) and CloudSat, and can be divided into three conceptual algorithmic blocks, which contain two stages of machine-learning (see Fig. 1). In the first algorithm block the two satellite datasets are combined into the partly labelled CUMULO dataset [20] to perform cloud classification of pixels in MODIS images resulting in a large set of physical variable retrievals together with cloud labels. In the second block, this labelled dataset is coarse grained and then used to train the second stage of the machine learning algorithm: a regression model used to transfer information obtained in the first block to other datasets such as the output from a climate model containing the same physical variables. In the third block, the regression model is applied to new unseen data, obtaining cloud class distributions, i.e. the percentages of each cloud type in each coarse grid cell of the dataset. This way, new datasets can be evaluated by relating these distributions to the underlying processes driving formation and evolution of the specific cloud type. We demonstrate the application of this method as a proof-of-concept using coarse grained data from

ESA Cloud_cci, showing the consistency of the approach on different and independent data.

B. Satellite data products

The cloud classes used in the CUMULO dataset are obtained from the 2B-CLDCLASS-LIDAR (Version P1-R05, [34]) product from CloudSat [37]. This product combines radar measurements from CloudSat and lidar data from the Cloud-Aerosol Lidar with Orthogonal Polarization (CALIOP) of the Cloud-Aerosol Lidar and Infrared Pathfinder Satellite Observation (CALIPSO) satellite [38] and uses them as the basis for a mixed threshold-based and fuzzy logic cloud classifier. One of the main advantages of combining radar and lidar products is a more robust determination of the thermodynamic phase of a cloud than would be possible by using lidar only. A limitation of the CLDCLASS-LIDAR dataset is its sparse coverage: measurements are provided in 0.16 s intervals with a footprint size of $(1.4 \times 1.8) \text{ km}^2$ [37]. The small footprint size also makes distinction between stratocumulus and stratus clouds difficult.

The inputs (called features in the following) to the machine-learning algorithms used here are also included in CUMULO and obtained from the MODIS instrument, which operates aboard the Terra and Aqua satellites. These are sun-synchronous polar-orbiting satellites like CloudSat and CALIPSO, which together with Aqua were part of NASA's afternoon constellation (A-Train) from 2006 to 2018, providing near simultaneous measurements. The data is taken specifically from the Level 2 MODIS Cloud Product [35] and the MODIS cloud mask using the most recent collection 6.1. The

MODIS Cloud Product data include nine pixel-level retrievals of physical variables (Table I) as well as 13 radiance channels. These variables are provided for images of 1354×2030 pixels with a resolution of 1 km. Each image covers five minutes. The cloud property retrievals provided by MODIS rely on the accuracy of the cloud mask and the cloud phase detection. The MODIS cloud mask is "clear-sky conservative", i.e. retrievals are only attempted for *probably cloudy* and *cloudy* pixels. Furthermore, the determination of the thermodynamic phase depends on the waveband used. Known limitations include increased uncertainties in the detected cloud phase in high elevation regions, including Greenland and Antarctica. We use the CUMULO dataset provided for the year 2008.

For validation of the method, we use version 3 of the ESA Cloud_cci data [39]. The ESA Cloud_cci data is a long-term cloud product data obtained from different observational sources. We use the dataset based on data from the Advanced Very High Resolution Radiometer (AVHRR) aboard the polar orbiting afternoon satellites from the National Oceanic and Atmospheric Administration (NOAA). Among others, the retrieved variables include a cloud mask and those that are available from the MODIS Cloud Product (Table I). Additionally available radiative fluxes are not used here. There are two different versions of the cloud variables available for different temporal resolutions. The L3C dataset provides monthly averages at 0.5° resolution, whereas the L3U dataset provides daily instantaneous measurements on a 0.05° grid. The effective emissivity ($ceff$) is only available for the monthly mean (L3C) data. The retrievals included in the Cloud_cci data are obtained using the Community Cloud retrieval for Climate (CC4CL) algorithms [40]. CC4CL shows little dependence on the observational instrument or the surface properties of the measurement region, but still suffers from some particular issues for retrievals using passive sensor data. This includes difficulties in assessing the thermodynamic phase of mixed-phase clouds as well as the detection of thin cirrus clouds. For this work, we used the the L3U dataset for June 2009 up to and including December 2011, with July 2010 being removed due to faulty temperature retrievals.

C. Cloud classification using MODIS and CloudSat data

First, we create the fully labelled version of CUMULO with cloud class labels for every cloudy pixel. The classes are obtained using a high-resolution, semisupervised pixel-wise classification scheme based on eight cloud classes as defined by the WMO. This makes the results more easily comprehensible because typical cloud properties are expected for each of these classes. Using an unsupervised or regime based method for this first stage would result in new classes or regimes with coarsely defined properties, respectively, thereby making the output more ambiguous and more difficult to interpret. The classification scheme applied here is largely based on the CUMULO dataset and classification algorithm by [20], which combines radiances and retrievals of physical cloud properties from the MODIS Cloud Product with the CLDCLASS-Lidar products from CloudSat. The CUMULO dataset provides one of eight cloud class labels (see Table II) per cloudy pixel along a narrow, vertically resolved swath of the CloudSat data which is collocated with the MODIS data. To be comparable to the

TABLE I: Physical variables available from the MODIS Cloud Product, usable as features for the machine learning models.

Abbv.	Physical variable
<i>cwp</i>	Cloud water path
<i>cod</i>	Cloud optical thickness
<i>ptop</i>	Cloud top pressure
<i>htop</i>	Cloud top height
<i>ttop</i>	Cloud top temperature
<i>tsurf</i>	Surface temperature
<i>cer</i>	Effective cloud particle radius
<i>ceff</i>	Effective Emissivity
<i>phase</i>	Cloud thermodynamical phase

TABLE II: Abbreviations in the CUMULO data.

Abbv.	Cloud type
Ci	Cirrus/Cirrostratus
As	Altostratus
Ac	Alto cumulus
St	Stratus
Sc	Stratocumulus
Cu	Cumulus
Ns	Nimbostratus
Dc	Deep Convection

2-dim MODIS data, each vertical column of the CloudSat cloud classes is labelled with the class which occurs most often in the respective vertical column. The data from the two satellites are aligned such that, where available, the label track from CloudSat is superimposed on the corresponding MODIS data (see example in Fig. 2). This excludes nighttime measurements, as some MODIS retrievals are not available at night. Since the CloudSat swath is quite narrow, most of the pixels in the resulting CUMULO dataset are not assigned a label, which is why a neural network is trained on the labelled part of the dataset to predict cloud class labels for the unlabelled pixels, which make up the majority of the dataset. The neural network used in [20] to classify clouds in the CUMULO dataset is a semisupervised convolutional network based on the invertible residual network (IResNet) [41] and can be trained on both the MODIS radiances as well as the MODIS Cloud Product retrievals included in the CUMULO dataset. The training is semisupervised, as the model learns to minimize the label entropy for unlabelled parts of the image in addition to the cross-entropy for the labelled parts. The IResNet is applied to tiles consisting of 3×3 MODIS pixels to determine the cloud type of the central pixel. During training, the output is the cloud class that occurs most often in the tile. If multiple cloud types occur equally often, one of them is chosen at random. Note that this way, the class label is predicted such that it is representative of the whole tile, even though the label is only assigned to the central pixel. This is a design choice that possibly introduces a bias towards more frequent cloud classes but increases the amount of usable tiles both for training and prediction by allowing for overlapping tiles. Tiles that contain less than six cloudy pixels according to the MODIS cloud mask are treated as undetermined and discarded. Therefore, the neural network is agnostic to such undetermined cases including clear sky situations. By applying the trained model, pixels in the CUMULO data that are yet unlabelled are assigned class labels, resulting in a set of fully labelled satellite data.

The CUMULO data contain MODIS radiance channels as well as retrieved physical cloud properties (Table II). With potential

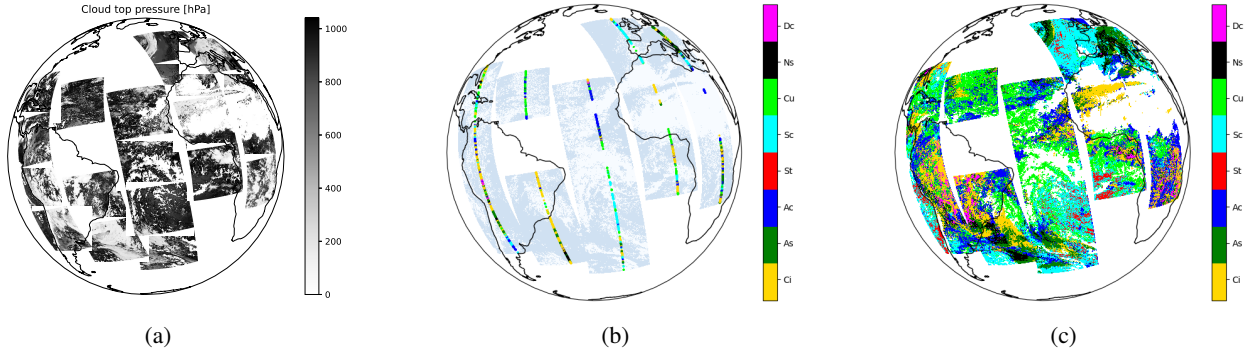


Fig. 2: One day of CUMULO data. 2a: Cloud top pressure $ptop$ as an example for one of the MODIS variable retrievals. 2b: the CloudSat label track (colors) superimposed onto the MODIS cloud mask (gray shading). 2c: results of the NN prediction, showing consistent cloud field across the borders of individual images. Not all orbits are complete because of unavailable data or failed alignment of MODIS and CloudSat.

application to climate models in mind, we decided to train the IResNet using the physical variables as features, these being more readily available from climate models than the radiances at the particular MODIS spectral channels. We found that the classes predicted by the model trained on the physical variable features were slightly more physically consistent. For example, we found that a number of high and thin clouds were given the Cumulus (Cu) label when using the radiances only, but this did not happen when using the physical cloud properties. However, the performance difference was marginal such that the classification step can be trained on either set of features. To be able to perform the training on physical variables, pixels containing missing values e.g. from failed MODIS retrievals are imputed, using the mean value for each 3×3 pixel tile. As the tiles are small, this is not expected to skew the values in the individual tiles significantly as neighboring pixels are expected to have similar properties.

In the following, the IResNet is trained on all available CUMULO granules for the year 2008 (~ 48000 multivariate images of 1354×2030 pixels) with standardized features. Instead of using a train/test split, we used 5-fold cross-validation on the same data to assess generalizability to unknown data. The model used for final predictions is then trained on the complete year. Due to high temporal resolution of the data, there should be enough variance in the features for the training data to be representative of longer periods typical for climate models. This will compensate for the fact that only one year of training data is used.

D. Information transfer to coarse data

The goal of the proposed method is to evaluate the representation of clouds and cloud-relevant processes in ESMs, for which the output differs significantly from the (labelled) satellite data in terms of temporal and spatial resolution. Furthermore, the ESM output does not necessarily contain the same variables as those included in the CUMULO dataset (observed radiances and/or retrieved physical variables). In order to bridge this gap, the information contained in the cloud-labelled satellite data has to be transferred to the ESM output domain. For this, we employ a second machine learning stage that can be trained

on the fully labelled satellite data and subsequently applied on new data.

For this to work, the horizontal resolution of the two datasets has to be matched more closely, which is done by coarse graining the labelled satellite data obtained from the pixel-wise classification. The satellites providing data for the CUMULO dataset are polar orbiting satellites making temporal coverage dependent on the geographical location. Here, we do not attempt to align the datasets temporally or use temporal averaging. Instead, we analyse the impact of applying the model trained on instantaneous satellite data from CUMULO onto temporally averaged target data.

All variables that are provided in both the CUMULO and the target dataset can be used as features. These are spatially coarse grained by creating cells of pixels in the source data such that the cell area roughly corresponds to the target data (e.g. model output) resolution. The labelled data are provided on an evenly spaced metric grid, but many climate models are provided on evenly spaced angular grids. The area covered by individual pixels will not match between these two grids and scale differently depending on the location. For simplicity and for the purpose of a proof-of-concept, we determine the grid cell size that is most representative of the target grid and use the averages of each variable over these grid cells as features for our model. We assume that the remaining differences between the grids are mitigated by averaging. The output is the relative cloud class occurrences in the grid cell, i.e. the fractional amount of the occurrence of each of the eight cloud classes plus the additional “undetermined” class for pixels that could not be assigned any of the predefined cloud classes. The “undetermined” class contains all pixels for which the prediction of a label was not possible due to failed MODIS retrievals, which often indicates clear sky. Missing values for pixels with no cloud are processed accordingly when computing the grid-cell averages (see section II-F), such that cloud class fractions are predicted consistently for all properties including those that are only defined for cloudy pixels (e.g. $ptop$). All grid cells containing only “undetermined” pixels are not included in the model training. Thus, we obtain a multivariate regression problem with a nine dimensional output space, containing the eight classes plus undetermined pixels, and

up to eleven features (i.e. the number of suitable physical variables provided by the CUMULO data, see section II-F). For our model, we choose the random forest (RF) [42] regression method for reasons of simplicity, computational efficiency, as well as its inherent normalization of the predicted fractions. After training the RF on the coarse-grained classified images, it can be directly applied to the target data, i.e. ESM output, providing cloud class fraction prediction for each grid cell. In order to investigate the sensitivity to the resolution and choice of features used, we trained multiple RFs for different respective choices. The individual training samples are weighted with weights w_i given by the L^1 -norm $w_i = \|\mathbf{y}_i - \bar{\mathbf{y}}\|_1$, where \mathbf{y}_i denotes the cloud class fractions for the i -th training sample and $\bar{\mathbf{y}}$ the average over all samples used in training. The weighting ensures that samples close to “the average sample” are given less weight in training, to reduce the effect of any bias in the data. We have about 48,000 labelled CUMULO granules (multivariate images of 1354×2030 pixels) available. In order to limit the amount of memory required, the RFs are trained on roughly $50 \cdot 10^6$ random samples drawn from a training split of 10000 labelled data images. The amount of samples varies because grid cells containing only “undetermined” pixels are excluded from training. The models are then evaluated on a test split of the data containing 8422 images. The hyperparameters of the RF models are chosen such that the depth of the individual regression trees is seventeen or less. We apply a bagging subsampling fraction of 0.7 and a minimum leaf size of 2, with 400 individual trees per forest. These hyperparameters showed an optimal trade-off between model’s performance and size.

E. Application and evaluation using ESA Cloud_cci data

As a proof-of-concept, we apply our method to an independent satellite dataset, the ESA Cloud_cci (ESACCI) data (see Section II-B). Note that application to satellite data is not the actual purpose of our method as pixel-wise classification would be more useful in this case. Application to the output of current ESMs (e.g. those contributing to CMIP6) is not yet possible due to too coarse horizontal and/or temporal resolution of the available output and/or key variables (e.g. *cer*, *cod*), required for sufficient performance, being unavailable. Therefore, independent satellite data are a well-suited proxy to test the applicability of our method. With the ESACCI data, coarse grained to a similar resolution as the typical output from ESMs, it can be shown that the method generalizes to coarse data obtained from different sources and it is expected to also be applicable to other similar datasets.

To perform an evaluation of the target data, the cloud class distributions obtained as described in section II-D can be used as reference. We show that the analysis of regional features of these classes, as well as of the feature value distributions conditioned on the cloud class fractions, are well suited to assess how well the target data represent observations. We propose to use this kind of analysis as a basis for process-oriented model evaluation through identification of specific cloud types. This can subsequently be used to assess and eventually improve key processes driving the formation and evolution of the different cloud types in ESMs. The ESACCI data provide a similar representation of the observed cloud

state and contain similar physical cloud variables as the MODIS product and are therefore comparable to the CUMULO data. In contrast to using ESM output as target data, this allows for a more direct assessment of uncertainties and limitations of this approach as possible model deficiencies do not play a role. The regression model trained on the coarse grained CUMULO data is applied to several instances of the ESACCI data with different coarse graining resolutions. This allows us to estimate the minimum spatial resolution required for a sensible evaluation of clouds in ESMs. In order to analyse the impact of the temporal resolution of the target data on the results, we use two-point daily means calculated from ascending and descending orbits of the ESACCI daily data. Predictions on these ESACCI instances are then compared to the predictions using instantaneous (i.e. not time-averaged) values. For each validation experiment using the coarse grained ESACCI data, we randomly sample 20% of the available grid cells.

F. Features and preprocessing

The RF regressor is trained on the features also available in the target dataset. For the ESACCI data, these include cloud top temperature (*ttop*), cloud top height (*htop*), cloud top pressure (*ptop*), surface temperature (*tsurf*), cloud optical thickness (*cod*), cloud water path (*cwp*) and the effective radius of cloud particles (*cer*). For the cloud water path and the effective radius the MODIS cloud product as well as the ESACCI daily product do not distinguish between ice and liquid water. Instead, an additional flag is available to distinguish between liquid and ice cloud tops, which we use to separate *cwp* into liquid water path (*lwp*) and ice water path (*iwp*) as well as *cer* into the liquid and ice particle radii (*cerl/ceri*). This procedure is an approximation and only justified under the assumption that the phase flag provided by the satellite data is representative for the whole cloud column. This will not be true for cases where several cloud types are overlapping, as MODIS can only report on the phase of the topmost cloud layer. The grid box averages for the cloud liquid/ice water path, the radii, *cod* are computed over all pixels in each cell, i.e. replacing missing values with zero. This is useful as these values approach zero with decreasing cloud amount. In contrast, *ptop*, *htop*, *ttop* are only averaged over cloudy pixels (“in-cloud values”). The features used for the RF model should ideally provide complementary information. Information on the cloud thickness is implicitly contained in *cwp* and *cod*. As the features *ptop*, *htop* and *ttop* effectively contain the same physical information, only one of them is used. Here, we use *ptop* as feature. In addition to the cloud variables, we also use surface temperature *tsurf* as it is readily available in many datasets. As a default, we therefore select *cwp*, *lwp*, *iwp*, *cerl*, *ceri*, *cod*, *ptop*, *tsurf*, which we call the *optimal set* of features in the following.

The ESACCI dataset also provides a pixel-wise uncertainty estimate for each variable, which we use to exclude pixels for which the uncertainty is larger than twice the actual value. We note that *cwp* in the ESACCI data can take very large values. Such outliers with *lwp* > 2000 g/m² or *iwp* > 6000 g/m² are excluded from the prediction. The arithmetic means of the latitude and longitude coordinates of all pixels in a grid cell are used as representative geographical location.

TABLE III: Fractions of the cloud classes for pixel-wise classification with prediction accuracy and F1 score for the supervised part of the data. CloudSat labels are for $21 \cdot 10^6$ labelled pixels included in CUMULO, predictions are for $800 \cdot 10^6$ pixels. Scores are averages for the 5 validation folds.

	Ci	As	Ac	St	Sc	Cu	Ns	Dc
CloudSat fraction	0.259	0.132	0.112	0.021	0.313	0.065	0.082	0.015
Predicted fraction	0.154	0.10	0.180	0.027	0.353	0.014	0.134	0.041
Prediction accuracy	0.85	0.84	0.88	0.95	0.78	0.91	0.90	0.98
Prediction F1-Score	0.64	0.40	0.44	0.21	0.66	0.46	0.48	0.48

III. RESULTS

A. Predicted cloud classes at pixel level

Since the pixel-wise cloud classification provides the basis for a process based analysis, it is crucial to ensure that the classes predicted by the IResNet model are physically consistent with the WMO labels. To assess the performance of the cloud classification we take into account the overall accuracy as well as the F1-score on the supervised portion of the validation data (Table III). Furthermore, we do a qualitative analysis of the physical properties of the predicted cloud classes to evaluate the consistency of the results.

The labels extracted from CloudSat that are available in CUMULO display a strong class imbalance (Table III), which we also find in the predicted classes. Most classes occur with a similar frequency in the source data and predictions, with deviations being small enough to be attributable to real differences in the data. We would like to highlight two key properties of the class distributions: (1) there are very few stratus (St) and deep convective (Dc) clouds in both the source and the prediction. (2) Cumulus (Cu) and cirrus (Ci) clouds are strongly underestimated in the predictions compared to the source data. For example, Cu has the smallest amount of all predicted cloud classes while this class is more common than St and Dc in the source data. Further assessment of the representation of these four classes (St, Dc, Cu, Ci) is therefore of high importance. The mean accuracy of the classification in the validation splits of the cross validation is larger than 0.8 for all classes but Sc, which suggests considerable skill of the classification method. However, for a multi-class problem with large class imbalance such as the one we have here, the accuracy alone is not a suitable measure to fully assess the performance of the method. We therefore additionally look at the F1-Score, which is sensitive to the class imbalance and can help identify individual class biases in the predictions. The F1-Score is at least 0.4 for all classes except for St, and especially high for Sc and Cu with values larger than 0.6. When considering the high accuracy scores for all classes, this suggests a good skill in representing the class imbalance. The lowest F1-Score is obtained for St (0.21) suggesting a rather low skill for this class. As noted in section II-B, the CloudSat algorithm has trouble distinguishing between St and Sc, which is why this is also to be expected for the IResNet. We demonstrate in our supplementary materials that the predicted classes are also physically consistent with the expectations of the respective WMO cloud types.

B. Cloud class distributions at coarse resolution

The RF is expensive to train and to evaluate on large datasets such as the year long, high-resolution CUMULO dataset. Because of these computational constraints, we train the Random

Forests on a subset of the labelled data of about 25% the size of the complete dataset. Tests have shown that the errors stabilize when using even fewer training data. The mean errors and R2 scores for the different settings are summarized in Table IV. Due to the fact that, with smaller grid cell sizes, more cells containing only “undetermined” pixels are excluded, the relative amount of cloudy pixels increases, which is why we see larger mean absolute errors for small grid cells. Using the median, however, we see better performance for smaller cells. The R2-score increases with grid cell size, most likely due to the decreasing variance caused by averaging over more pixels. The performance is therefore judged not to be strongly dependent on the grid box size, and we choose $(100 \text{ km})^2$ grid cells for most of the results shown here and in the supplementary material, as this is comparable to typical ESM resolutions. As these numbers alone do not provide a clear measure of how well the regression performs, we also use joint densities of predicted and ground truth cloud fractions of the test split as a performance indicator. Fig. 3 shows such joint densities for true and predicted fractions for a grid cell size of $(100 \text{ km})^2$ using the optimal set of features (see section II-F). The joint density plot displays the concentration of samples in the truth/prediction space, and along the x- and y-axis the marginal distributions of the true and predicted fractions, respectively. A perfect performance would result in a joint density plot in which all samples are aligned on the diagonal (indicated by red line) corresponding to a perfect linear correlation. For both cloud classes in Fig. 3, there is a clear correlation between the ground truth and the predictions. Many predictions are, however, far off the target: Fig. 3b shows several hundred samples with a predicted Ns fraction of about 0.2 where the true fraction is close to 1. For this specific example, this is a small fraction ($O(0.001\%)$) of the total number of grid cells, but it shows that the predictions can differ strongly from the true values in non-negligible number of cases. This deviation is a manifestation of ambiguity between different cloud states, likely caused by noise generated by the averaging of the features. Furthermore, this is an example of the predictions favoring low cloud fractions, as the “undetermined” class is quite prevalent in the training data. As shown in Fig. 3a, large altocumulus (Ac) fractions (> 0.9) are underestimated by the RF, but the deviation in this region remains largely below 0.1, as indicated by the dashed line. Most of the samples are, however, still contained within the $\Delta = 0.1$ range (magenta dashed lines). For fractions larger than 0.2, samples deviating by more than a factor of 2 (outside black lines) are rare. For fractions smaller than 0.2 (bottom left corner), deviations by a factor of more than 2 occur frequently, indicating difficulty to correctly predict small fractions. Note that such predictions contribute significantly to the relative

TABLE IV: Results of the regression models for different grid box sizes. (1): Trained using default set of features. (2): Using *cwp* and *cer*, not separated into ice and liquid, in addition to *cod*, *ptop*, *tsurf*. (3): Using (*cwp*, *cer*, *ptop*, *tsurf*) as features.

Grid cell size	Mean abs. error	Median error	Median relative error	R2-Score	Random MAE
3 km ⁽¹⁾	0.042	0.0018	18.9%	0.816	0.193
10 km ⁽¹⁾	0.036	0.002	33.9 %	0.836	0.178
20 km ⁽¹⁾	0.033	0.0025	41.3%	0.840	0.169
100 km ⁽¹⁾	0.027	0.0038	52.6%	0.845	0.151
200 km ⁽¹⁾	0.025	0.0045	54.2%	0.859	0.143
100 km ⁽²⁾	0.028	0.0041	55.4%	0.837	0.151
100 km ⁽³⁾	0.033	0.0043	60.4%	0.755	0.151

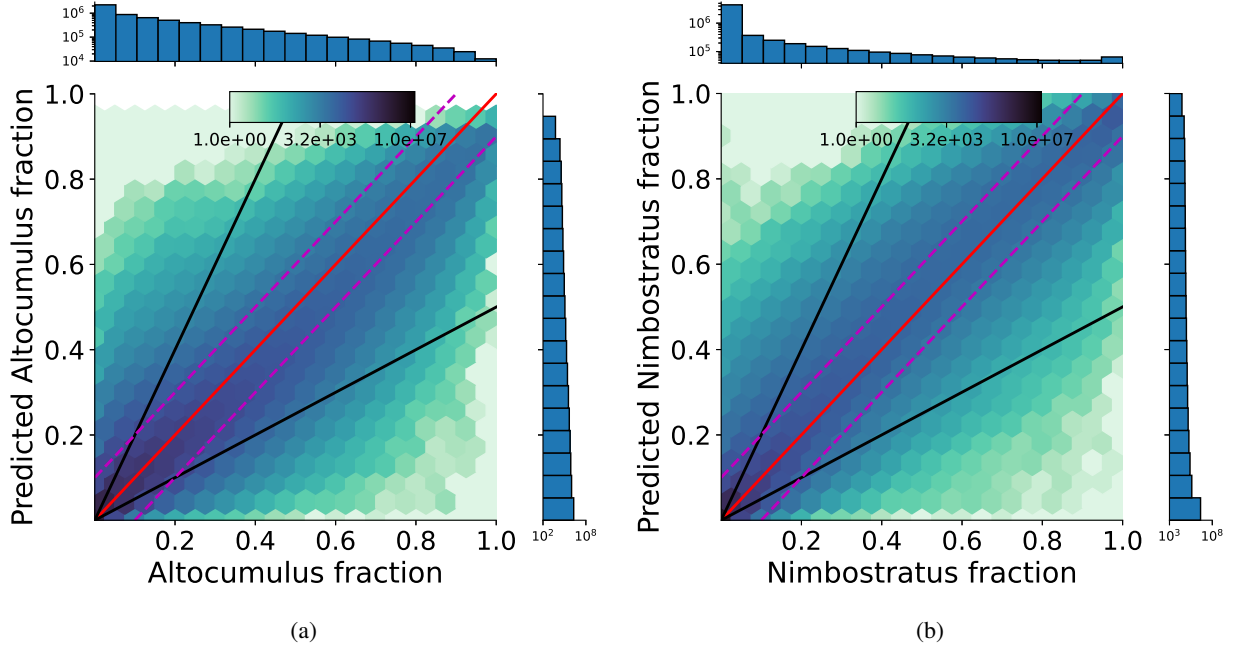


Fig. 3: Joint density of the predicted and true Ac (left) and Ns (right) fractions from the CUMULO test set for a grid cell size of $(100 \text{ km})^2$, using the optimal set of features (Section II-F). The color scale and the marginal histograms are logarithmic. The predicted fractions are in both cases clearly correlated to the ground truth values, with a Pearson correlation of $c_P = 0.96$ for Ns and $c_P = 0.89$ for Ac. The red line indicates the line of perfect correlation. The area between the dashed magenta lines indicate a deviation between ground truth and prediction of less than 0.1 and the area between the black lines indicates a deviation by less than a factor of two in either direction.

error, but have a negligible effect on the absolute error. To show that the model indeed has some skill, we compare the metrics shown in Table IV to predictions drawn randomly from the individual distribution of fractions in the source data. We find that the mean absolute deviation is larger for the random baseline by roughly a factor of five, indicating that the regression model clearly outperforms the random baseline.

In the supplementary materials to this paper, we show that our method reproduces physically meaningful cloud class distributions. Specifically, we show that the features resulting in a prediction of a certain cloud class are in line with those expected from the meteorological definition of the respective class.

As the variables available in typical ESM output can vary, not always matching our optimal set of features, we also determine which of these features are essential to achieve good performance. In addition to using the optimal set of features, we therefore also trained the model using different alternative

sets, containing fewer features. Using the cloud top phase flag to distinguish between ice and liquid for some of our features (*lwp*, *iwp*, *cerl*, *ceri*) produces a small performance increase as the metrics indicate in Table IV. Comparing Fig. 3a and Fig. 4a, shows that the correlation between the true and predicted values becomes less pronounced when the information about the thermodynamic phase is removed. Further ablation studies reveal, that using *cod* and *ptop* is critical for the RF performance, but these variables are infrequently contained in ESM standard output. An example is shown using features without *cod*, where Table IV shows a significant decrease in the R2-score. The effect on the joint density displayed in Fig. 4b is visible as predicted fractions being skewed towards smaller values. Predicted fractions above 0.8 are very rare and the joint density seems to be shifted towards the lower black line, corresponding to half the true value. We provide further information on the feature importance in the supplementary materials.

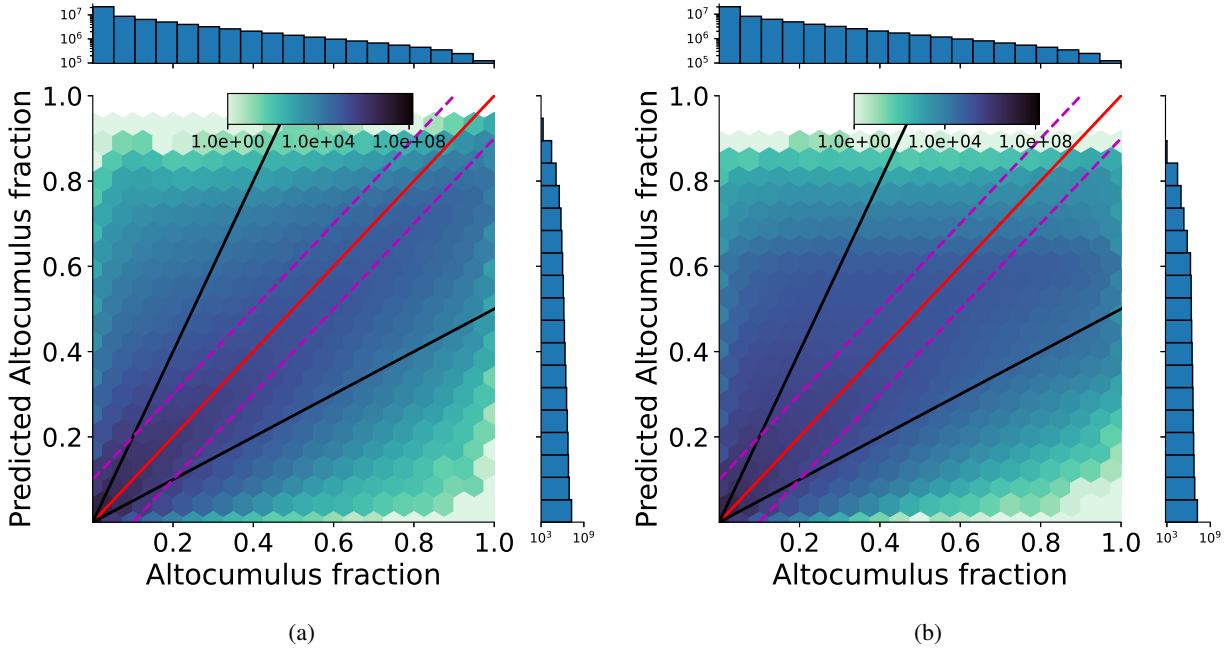


Fig. 4: Results for a model trained using features without liquid/ice distinction (*cwp*, *cer*, *cod*, *ptop*, *tsurf*) (4a) versus a model trained also without *cod* (4b). Without information on the thermodynamic phase the model skill is slightly reduced compared to Fig. 3, but further removing the cloud optical thickness from the features reduces the performance considerably.

C. Validation using alternative satellite data

In order to assess the generalization performance of the method we compare predictions of the class distributions on ESACCI data to the classes from the CloudSat CLDCLASS-LIDAR product. We use the class labels from CloudSat for the year 2008, which were also used for the CUMULO dataset. Again, the 3-dim CloudSat data are aggregated to two dimensions by using the most common cloud class within each vertical column as representative cloud class. If several cloud classes occur equally often, one of them is chosen randomly. The labels provided by CloudSat for individual orbits are relatively sparse, but using a whole year of measurements allows for evaluating how well the predictions from the RF models on the ESACCI data match the CloudSat distributions. Fig. 5 shows that even though the data have been aggregated to coarse grid cells of $2^\circ \times 2^\circ$, the relatively sparse availability of CloudSat data is still apparent. Consequently, clear regional differences are not visible for all cloud classes, but Ci, Sc and Cu show distinct areas of frequent occurrence. For example, Sc clouds are frequently detected in the subtropical subsidence regions off the west coasts of the continents, Ci clouds are frequent in the deep Tropics, Cu are found frequently over the tropical and subtropical oceans away from the stratocumulus decks.

In the following, for better comparison of the CloudSat ground truth and the predictions on the ESACCI data, we exclude the “undetermined” predictions such that the cumulative fraction of all eight cloud classes equals one in each cell. The reported fractions are therefore a relative measure and independent of the total cloud amount in each grid cell.

The CUMULO and the ESACCI data are provided on different grids. Because of averaging, same size grid cells are not

needed and thus no interpolative re-gridding is applied. In order to assess possible effects of different grid cell sizes, we compare predictions obtained with the same model on differently sized ESACCI grid cells in the supplements to this paper. Our results show that for a model trained on large $(100 \text{ km})^2$ grid cells, there is no qualitative difference in the predictions for different grid sizes. For this reason, (100×100) pixel grid cells are used in the following for most of the results shown here, corresponding to $5^\circ \times 5^\circ$. However, some features become more pronounced when smaller grid cells are used during prediction. The maximum grid cell size for a reasonable application to ESM output therefore depends on the region or processes of interest.

To determine if the method can correctly capture specific meteorological conditions, we look for robust characteristics in the regional and temporal distribution of the classes. Fig. 6 shows the predictions on the ESACCI data using the RF trained on grid cells of $(10 \text{ km})^2$ and applied 10×10 pixel grid cells. These results show that the different classes show very distinct pattern of occurrence across the globe. This means that using this method, different regions can be analysed with respect to the characteristic cloud classes expected there. Furthermore, it clearly shows that the Sc class dominates in the predictions, while St and Dc occur very rarely. This means that an analysis should be conducted by taking into account the relative occurrence of the same class in different areas instead of comparing classes to each other.

In order to assess the temporal evolution and seasonal cycle of the predicted cloud classes, Fig. 7 shows the time series of the class fractions averaged over grid cells in the Southern Hemisphere for which the respective cloud class can vary strongly. We chose to determine this by selecting grid cells for each class where at some time the class fraction is especially

Relative cloud class occurrence

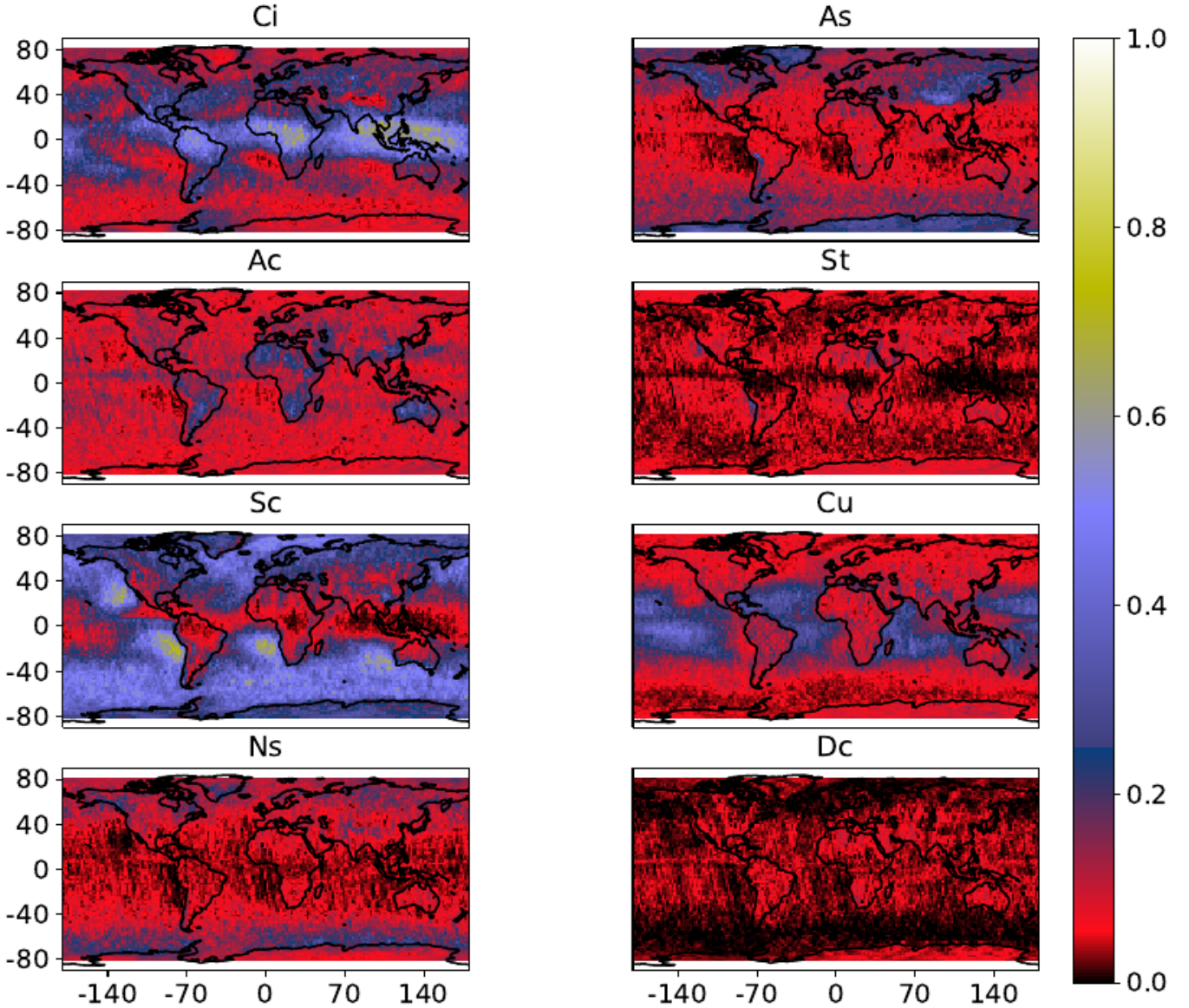


Fig. 5: Relative occurrence per class from CloudSat measurements (2008) from the 2B-CLDCLASS-LIDAR product binned to $2^\circ \times 2^\circ$ grid cells.

large (90th percentile). Only the Southern Hemisphere is selected to avoid the north and south cancelling each other out. Using this method of analysis, almost all predicted classes show a seasonal cycle. Only for the classes Cu and Sc such a cycle is not clearly visible. The Ns and As classes are predicted at higher fractions in the cold months. In contrast to Ns and As, Ac and St have higher fractions in summer. The CloudSat ground truth is too sparse to similarly assess seasonal cycles and enable a direct comparison. But the fact that these cycles exist in our predictions without being explicitly learned reinforces the notion that the method can distinguish clouds meaningfully. As a consequence, seasonal cycles should be expected when the method is applied to ESM output and a possible absence of these cycles would indicate deficiencies

in the cloud representation of the model.

D. Uncertainty estimate

For the ESM evaluation, deviations introduced by the data need to be separable from those caused by the evaluation method. We therefore provide an estimate of the uncertainty introduced by our machine learning models. This will help in attributing deviations larger than this uncertainty to specific model deficiencies. In order to obtain an uncertainty estimate for the consecutive application of both machine-learning methods and for a more quantitative comparison between the predictions and the CloudSat ground truth, we compute the Pearson correlation and difference between the

Mean cloud-type fractions

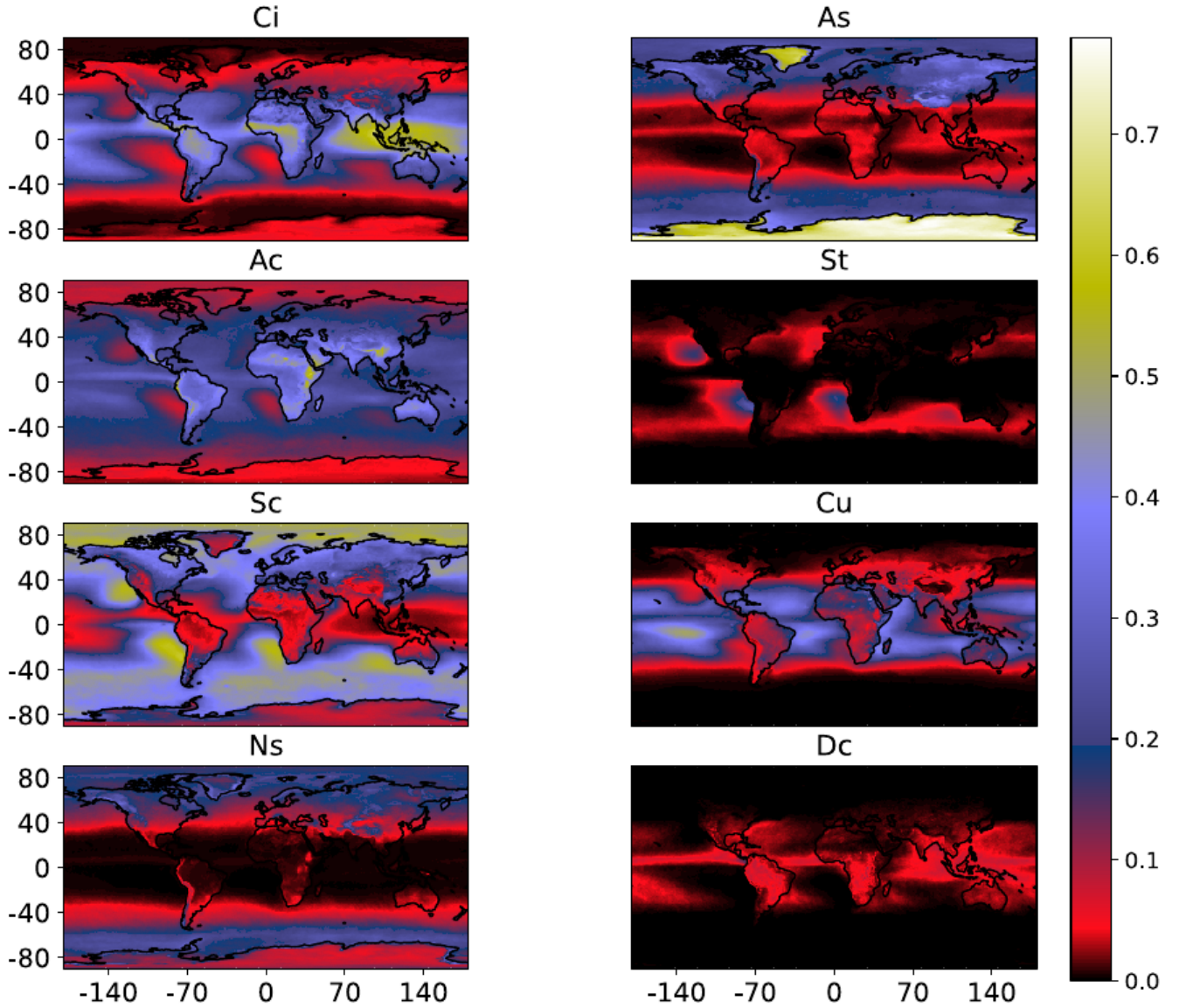


Fig. 6: Average class fractions for the predictions on the ESACCI data binned to a $1^\circ \times 1^\circ$ grid. Underlying RF trained on $(10 \text{ km})^2$ grid cells from the complete labelled dataset and applied to 10×10 pixel ESACCI grid cells. Many classes show similarities to the distributions in the CloudSat data (Fig. 5), even though the location is not used as a feature.

predictions and the CloudSat labels. For this purpose we bin the relative amount of each class to grid cells of $2^\circ \times 2^\circ$ size for both datasets. As an example, differences for the cloud types with highest (Cu) and lowest (St) correlation are shown in Fig. 8. The difference increases with the fraction of occurrence of each class (as displayed Fig. 6). Note that this is only a rough measure for accuracy as the two datasets differ in temporal and spatial resolution. Additionally, an exact match cannot be expected as the CloudSat data cover the year 2008, while the ESACCI data used cover the time period June 2009 to the end of 2011. The mean within-class correlation is 0.65, indicating a moderate similarity between

the regional distribution of the classes in CloudSat and the predictions. Regional phenomena found in the predicted class distributions are therefore in qualitative agreement with the ground truth. Table V shows the mean fractions of the classes in the predictions and the CloudSat data. The predictions here are comparable to the pixel-wise predictions obtained using the IResNet (Table III). The most notable difference in the distribution is again the under-representation of Ci in the predictions relative to the CloudSat labels, which is caused by the under-representation in the predicted pixel-wise labels. Table V also shows the relative difference between the two distributions for grid cells showing a large class fraction in

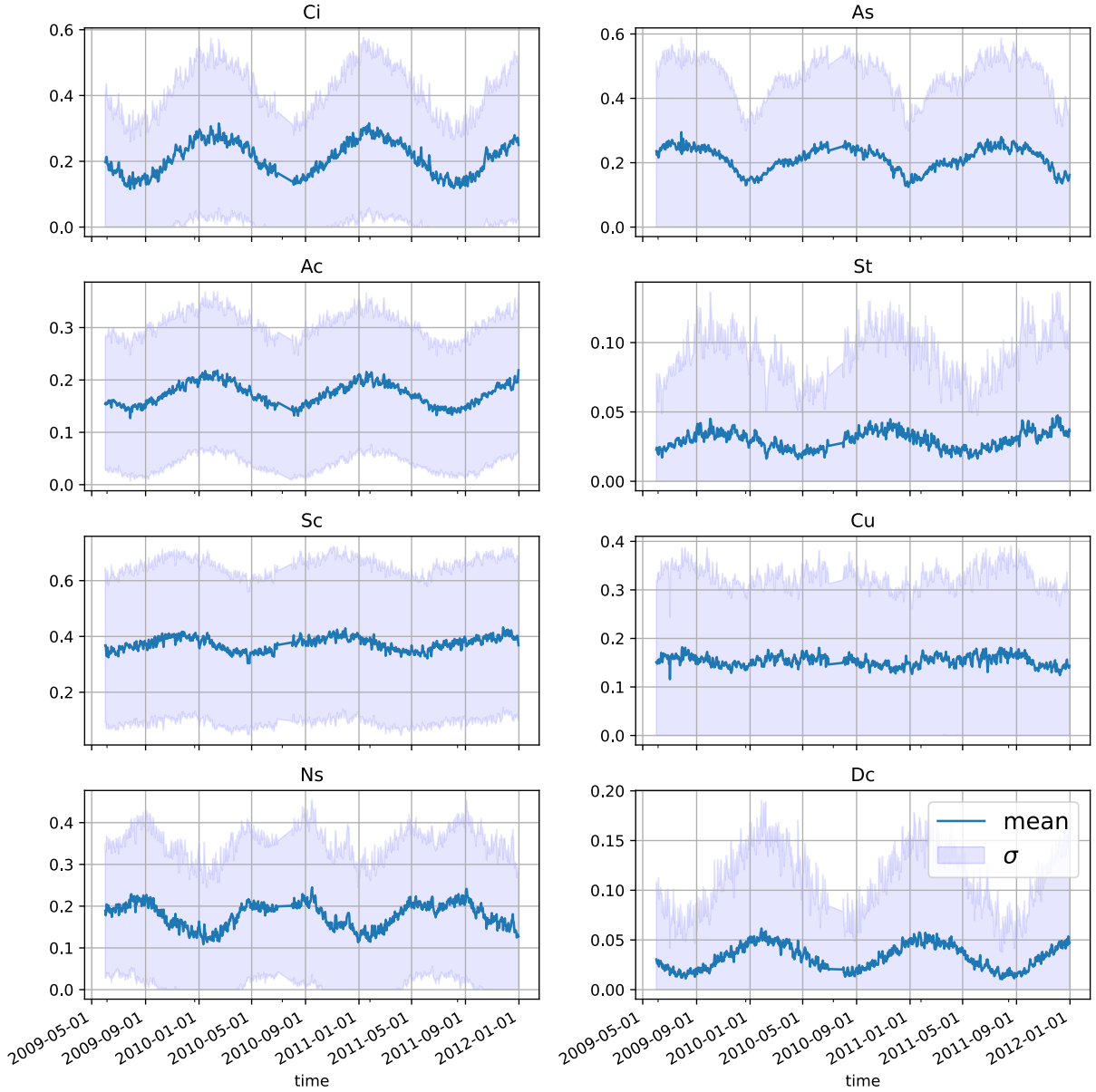


Fig. 7: Time series of mean predicted class fractions from 1 June 2009 to 31 December 2011. The per-class mean is computed for all locations in the southern hemisphere where at least one instance of the respective cloud class fraction is within the 90th percentile of all predictions of this class. Note that July 2010 has been excluded due to faulty data.

the predictions (90th percentile). These are the grid cells, for which the accuracy of the prediction is especially important because they have a large influence on the qualitative results. For all classes the magnitude of this deviation is below 50%. This is also the range of relative deviation we found on the test split, leading to an overall estimate of the uncertainty of 50%.

IV. SUMMARY AND DISCUSSION

We presented a method for the evaluation of clouds in coarse resolution data, employing consecutive application of machine-learned classification and regression models. Using this method, information on clouds from high-resolution, three-dimensional CloudSat and CALIPSO lidar products is

TABLE V: Mean fraction of the predicted classes compared with the relative amounts of the classes in CloudSat. The last row shows the mean difference for pixels with predictions in the 90th percentile Δ_{90} relative to the mean μ_{90} of these predictions. Predictions are taken from a model trained on the default set of features using $(100 \text{ km})^2$ and applied on 100×100 pixel ESACCI grid cells.

	Ci	As	Ac	St	Sc	Cu	Ns	Dc
Predict.	0.13	0.14	0.19	0.01	0.31	0.10	0.10	0.02
CloudSat	0.20	0.13	0.11	0.05	0.27	0.12	0.09	0.03
c_P	0.87	0.80	0.60	0.18	0.88	0.84	0.83	0.36
Δ_{90}/μ_{90}	-29%	49%	49%	1%	18%	14%	30%	39%

first added to passive sensor data from MODIS by using the

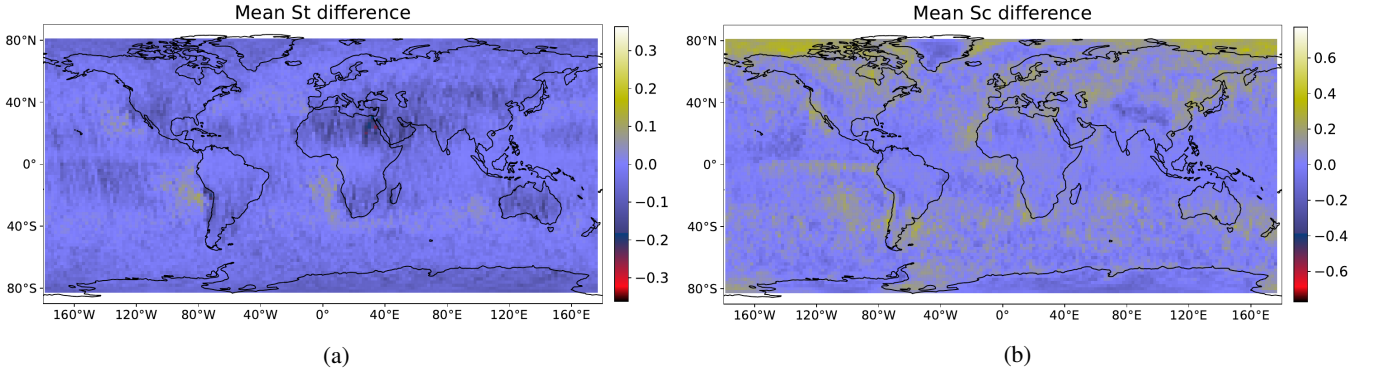


Fig. 8: Difference between the mean predicted fractions and CloudSat per $2^\circ \times 2^\circ$ grid cell for the relative amount of the classes with lowest/highest correlation, St (8a, $c_P = 0.18$)/Sc (8b, $c_P = 0.88$). The colormap is normalized to the range $[-m, m]$, where m is the maximum value for the class across both (CloudSat, predictions) distributions. Predictions obtained from RF trained on $(100 \text{ km})^2$ data and applied on 100×100 ESACCI pixels.

CUMULO framework, and then transferred to coarse resolution data. This approach offers a new perspective on statistical and process-oriented assessment of the performance of climate models. The presentation of the model output in terms of different cloud classes exposes the different driving mechanisms for formation and evolution of the clouds more clearly, allowing for a process-oriented analysis. This provides the potential to better understand and ultimately improve existing model deficiencies.

The pixel-wise classification has a high accuracy of at least 80% for each individual class. The relative amounts of predicted Cu and St, however, can differ by more than a factor of 2 compared to the CloudSat data used as ground truth. The deviations in the amount of St can be at least partly explained by the relatively small amount of training samples and the similarity to the physical properties between St and Sc. Since the predicted cloud classes show distinct physical properties that are consistent with the expected properties of the corresponding WMO cloud classes, we argue that these results can still be meaningful. We conclude that pixel-wise labelled data are therefore suitable as a basis for training a regression model which learns cloud class distributions on datasets with a horizontal resolution typical for climate model scales.

We could further show that this subsequent regression can reproduce consistent cloud class distributions on regional scales with mean errors being at least one order of magnitude smaller than the random baseline. Furthermore, the RF regressor successfully generalizes to different data as could be shown using the ESACCI data. The predicted global distributions of the individual cloud classes compare well with the CloudSat ground truth. This is evident when qualitatively comparing the distributions for each class as well as in the correlations and difference in areas of high class fraction. The correlation is larger than 0.6 for all but 2 classes (St/Dc) and the relative difference in areas of high class fraction is smaller than 50% for all classes. The spatio-temporal location of a sample is not used as an input for the machine-learning algorithms. Therefore, any predictions are solely based on the physical properties represented by the features. Yet, even small-scale regional characteristics of

the CloudSat ground truth are similarly represented in the predictions using the ESACCI data. Notable examples are a peak of Ci in the tropical warm pool region or an increased As fraction in the Himalayas. Additionally, the geographical means for all classes correlate positively with the respective relative occurrence in the CloudSat ground truth, with higher correlations for the classes with many available samples. From this we conclude that the pixel-wise classification is capable of providing a sufficient substitute for spatio-temporal locations where CloudSat data are not available. We further showed that the regression model associates each class with specific feature values (see supplements). These values are consistent with the expected properties of the different WMO cloud types. These results suggest that the method is suitable for a process-oriented assessment of clouds simulated by climate models. However, due to the nature of the multi-stage process some limitations apply: by building the regression on two dimensional, spatially averaged source data it is hard to make correct predictions on individual grid cells. This results in a number of samples for which the predicted cloud fraction differs by a factor of 2 or more. Additionally, the under-representation of the Cu class and the limited accuracy of the St class show that this method can still be improved.

Further analysis of the sensitivity of our method to temporal averaging of the target data showed that the method works well with near instantaneous data but cannot be applied to monthly averaged data (see supplements). This is possibly caused by skewing of feature value distributions. Using geostationary data available e.g. every 30 minutes (GOES satellite, [43]) for the pixel-wise classification instead of MODIS data available only twice a day might improve the results. Such an approach has been applied to other atmospheric variables like convection and rainfall [44], [45]. The physical properties of the predicted clouds could then be safely averaged over time due to the high and consistent temporal resolution of the data allowing the regression model to train on data more comparable to typical ESMs output. However, the processes to be evaluated with our approach are not resolved at large temporal scales. This contributes to the poor regression performance for the monthly data and will still be an issue when the RF is trained on temporally averaged data. In turn, this means that this method

is suitable to detect model deficiencies relatively quickly in contrast to using climatological means from long simulations. This is because an inaccurate representation of the global or local cloud distributions can probably already be detected with model output available for less than a year.

We have tested our prediction method using multiple sets of input features and have found that information about the cloud height, its water content and its optical thickness are essential for good performance, with information on the thermodynamic phase of the cloud providing additional robustness. The horizontal resolution of the model seems to be less critical (see supplements). Models trained on different grid cell sizes show differences but no clear optimal resolution can be defined from these initial results, especially when the similarity to the resolution of the target data is taken into account. Predictions should be performed on data from the highest available horizontal resolution as more features can be resolved. Some features of the predicted cloud distribution such as, for example, the high fractions of Ns along the Antarctic coast, might be amplified or hidden by noisy satellite retrievals. Especially in the high latitudes clouds are challenging to identify with passive sensors like MODIS.

The consecutive application of two machine learning methods makes it difficult to quantitatively estimate the propagated errors. Even though the error of the classification and regression can be individually estimated using test splits, the combined impact of these errors is not clear. This is further complicated by possible inconsistencies in the CloudSat classification algorithm, i.e. clouds not being labelled the same way a human expert would. An example for this are the difficulties in differentiating between St and Sc. We do not, however, see any specific inconsistencies in the physical properties or the regional distributions of the predictions, suggesting that the propagated uncertainties are acceptable. Even for classes for which limited training data are available (Cu, St, Dc), we find that the predictions are self-consistent. This is apparent in the characteristic feature values, which are distinct for each class and do not vary regionally (see supplements). The regional distributions of the classes are in fact attributable to the predominant atmospheric conditions represented in the features. The Dc class occurs more frequently near the equator, Cu is found predominantly in tropical and subtropical regions above the ocean, St mostly west off the continents in the subtropical subsidence regions. Both, Cu and St are as expected low-level clouds with low cloud top heights.

Our findings suggest that this method can be successfully applied to any dataset of sufficient length and horizontal and temporal resolution to allow for statistically robust predictions. This is supported by the joint densities on the test data showing clear correlations of ground truth and predictions. Additionally, the predictions on the ESACCI data provide enough information to isolate individual features and processes. This provides the opportunity to analyse clouds on regional scales. This could for example be done for the low-level cloud fields west off the continents, investigating their horizontal extent, their dependence on the feature values and their temporal evolution. The method can therefore be used to identify spatio-temporal areas in which clouds are not correctly represented. On the test data, the median relative

deviation was about 50%. Comparing the predictions with the raw labels from CloudSat we find similar values. Especially for regions where specific cloud types are predicted with a high frequency, we find relative deviations mostly below 50%. Only the St class is consistently under-represented for which the pixel-wise classification already showed poor performance. For ESM evaluation, an uncertainty of at least 50% to what would be reported by CloudSat for individual predictions can be expected. However, in large datasets, the method can clearly highlight individual regions of high occurrence for a class. The absence or under-representation of such phenomena would be signs of possible ESM deficiencies. The St and Cu classes, however, cannot be predicted with much confidence. This probably stems from the CloudSat ground truth itself, as it has trouble distinguishing between St and Sc. We would therefore recommend combining these classes when applying this or similar methods.

In terms of implementation, this method can be applied to new datasets quickly and does not require individual implementation for each model. We would like to note that many of the variables needed for this method are typically part of the standard output of climate models so that the main requirement would be to provide instantaneous or near-instantaneous values, i.e. model output not averaged over longer time intervals. We would therefore like to encourage the modelling community to provide such an output e.g. in future model intercomparison projects such as CMIP7. We especially recommend to add the cloud optical thickness, and the effective particle radii for liquid and ice particles as instantaneous 2-dim variables to the CMIP7 data request in addition to the already available variables (*cwp*, *ctp*, *tsurf*). Future improvement of the method could include replacing the RF as a regression model. The most significant positive feature of the RF is the use of the bagging process during training, which helps to generalize well to unseen data. However, the size of the RF scaling with the size of the dataset and batched training not straightforward necessitates a high degree of subsampling to make training computationally feasible. Therefore, as noted previously, this required us to discard data. However, once trained, applying the RF to batched data for predictions is possible and fast, making it viable for practical application. Also, the CloudSat cloud classes in the source data are aggregated in the vertical dimension by assigning the most common class in the cloud column to the respective pixel. Even though this provides an implicit resolution of vertical features, a full classification in three dimensions would be a clear improvement. An improved representation of the vertical cloud structure might be obtained by using a more sophisticated aggregation algorithm. Taking into account the physical properties of the observed pixel in each vertical column might lead to a more representative ground truth.

REFERENCES

- [1] V. Eyring, S. Bony, G. A. Meehl, C. A. Senior, B. Stevens, R. J. Stouffer, and K. E. Taylor, "Overview of the Coupled Model Intercomparison Project Phase 6 (CMIP6) experimental design and organization," *Geoscientific Model Development*, vol. 9, no. 5, pp. 1937–1958, 2016.
- [2] V. Eyring, P. M. Cox, G. M. Flato, P. J. Gleckler, G. Abramowitz, P. Caldwell, W. D. Collins, B. K. Gier, A. D. Hall, F. M. Hoffman, G. C. Hurtt, A. Jahn, C. D. Jones, S. A. Klein, J. P. Krasting, L. Kwiatkowski, R. Lorenz, E. Maloney, G. A. Meehl, A. G. Pendergrass, R. Pincus, A. C. Ruane, J. L. Russell, B. M. Sanderson, B. D. Santer, S. C. Sherwood, I. R. Simpson, R. J. Stouffer, and M. S. Williamson, "Taking climate model evaluation to the next level," *Nat. Clim. Change*, vol. 9, no. 2, pp. 102–110, 2019.
- [3] P. P. Vignesh, J. H. Jiang, P. Kishore, H. Su, T. Smay, N. Brighton, and I. Velicogna, "Assessment of CMIP6 Cloud Fraction and Comparison with Satellite Observations," *Earth and Space Science*, vol. 7, no. 2, pp. 1–21, 2020.
- [4] T. A. Myers, R. C. Scott, M. D. Zelinka, S. A. Klein, J. R. Norris, and P. M. Caldwell, "Observational constraints on low cloud feedback reduce uncertainty of climate sensitivity," *Nature Climate Change*, vol. 11, no. 6, pp. 501–507, 2021.
- [5] M. J. Webb, T. Andrews, A. Bodas-Salcedo, S. Bony, C. S. Bretherton, R. Chadwick, H. Chepfer, H. Douville, P. Good, J. E. Kay, S. A. Klein, R. Marchand, B. Medeiros, A. Pier Siebesma, C. B. Skinner, B. Stevens, G. Tselioudis, Y. Tsushima, and M. Watanabe, "The Cloud Feedback Model Intercomparison Project (CFMIP) contribution to CMIP6," *Geoscientific Model Development*, vol. 10, no. 1, pp. 359–384, 2017.
- [6] P. Ceppi, F. Briant, M. D. Zelinka, and D. L. Hartmann, "Cloud feedback mechanisms and their representation in global climate models," *WIREs Climate Change*, vol. 8, no. 4, pp. 345–369, Jul. 2017.
- [7] M. D. Zelinka, T. A. Myers, D. T. McCoy, S. Po-Chedley, P. M. Caldwell, P. Ceppi, S. A. Klein, and K. E. Taylor, "Causes of Higher Climate Sensitivity in CMIP6 Models," *Geophysical Research Letters*, vol. 47, no. 1, pp. 1–12, 2020.
- [8] S. Bony, B. Stevens, D. M. Frierson, C. Jakob, M. Kageyama, R. Pincus, T. G. Shepherd, S. C. Sherwood, A. P. Siebesma, A. H. Sobel, M. Watanabe, and M. J. Webb, "Clouds, circulation and climate sensitivity," *Nature Geoscience*, vol. 8, no. 4, pp. 261–268, 2015.
- [9] T. Schneider, J. Teixeira, C. S. Bretherton, F. Briant, K. G. Pressel, C. Schär, and A. P. Siebesma, "Climate goals and computing the future of clouds," *Nature Publishing Group*, vol. 7, no. 1, pp. 3–5, 2017.
- [10] K. D. Williams and M. J. Webb, "A quantitative performance assessment of cloud regimes in climate models," *Climate Dynamics*, vol. 33, no. 1, pp. 141–157, 2009.
- [11] L. Bock, A. Lauer, M. Schlund, M. Barreiro, N. Belouin, C. Jones, G. A. Meehl, V. Predoi, M. J. Roberts, and V. Eyring, "Quantifying Progress Across Different CMIP Phases With the ESMValTool," *Journal of Geophysical Research: Atmospheres*, vol. 125, no. 21, pp. 1–28, 2020.
- [12] A. Lauer, V. Eyring, M. Righi, M. Buchwitz, P. De-fourny, M. Evaldsson, P. Friedlingstein, R. de Jeu, G. de Leeuw, A. Loew, C. Merchant, B. Müller, T. Popp, M. Reuter, S. Sandven, D. Senfteleben, M. Stengel, M. V. Roozendael, S. Wenzel, and U. Willen, "Benchmarking CMIP5 models with a subset of ESA CCI Phase 2 data using the ESMValTool," *Remote Sensing of Environment*, vol. 203, pp. 9–39, Dezember 2017.
- [13] Y. Wang, "Quantitative remote sensing inversion in earth science: Theory and numerical treatment," in *Handbook of Geomathematics*, W. Freeden, M. Z. Nashed, and T. Sonar, Eds. Berlin, Heidelberg: Springer Berlin Heidelberg, 2010, pp. 785–812.
- [14] D. J. Swales, R. Pincus, and A. Bodas-Salcedo, "The Cloud Feedback Model Intercomparison Project Observational Simulator Package: Version 2," *Geoscientific Model Development*, vol. 11, no. 1, pp. 77–81, 2018.
- [15] M. Righi, B. Andela, V. Eyring, A. Lauer, V. Predoi, M. Schlund, J. Vegas-Regidor, L. Bock, B. Brötz, L. de Mora, F. Diblen, L. Dreyer, N. Drost, P. Earnshaw, B. Hassler, N. Koldunov, B. Little, S. Loosveldt Tomas, and K. Zimmermann, "Earth System Model Evaluation Tool (ESMValTool) v2.0 – technical overview," *Geoscientific Model Development*, vol. 13, no. 3, pp. 1179–1199, 2020.
- [16] A. Lauer, V. Eyring, O. Bellprat, L. Bock, B. K. Gier, A. Hunter, R. Lorenz, N. Perez-Zanon, M. Righi, M. Schlund, D. Senfteleben, K. Weigel, and S. Zechlau, "Earth System Model Evaluation Tool (ESMValTool) v2.0 - Diagnostics for emergent constraints and future projections from Earth system models in CMIP," *Geoscientific Model Development*, vol. 13, no. 9, pp. 4205–4228, 2020.
- [17] V. Eyring, L. Bock, A. Lauer, M. Righi, M. Schlund, B. Andela, E. Arnone, O. Bellprat, N. Carvalhais, I. Cionni, N. Cortesi, B. Crezee, E. L. Davin, P. Davini, K. Debeire, L. De Mora, C. Deser, D. Docquier, P. Earnshaw, C. Ehbrecht, B. K. Gier, N. Gonzalez-Reviriego, P. Goodman, S. Hagemann, S. Hardiman, B. Hassler, A. Hunter, C. Kadow, S. Kindermann, S. Koirala, N. Koldunov, Q. Lejeune, V. Lembo, T. Lovato, V. Lucarini, B. Müller, A. Pandde, A. Phillips, V. Predoi, J. Russell, A. Sellar, F. Serva, T. Stacke, R. Swaminathan, J. Vegas-Regidor, J. Von Hardenberg, K. Weigel, and K. Zimmermann, "Earth System Model Evaluation Tool (ESMValTool) v2.0 - An extended set of large-scale diagnostics for quasi-operational and comprehensive evaluation of Earth system models in CMIP," *Geoscientific Model Development*, vol. 13, no. 7, pp. 3383–3438, 2020.
- [18] K. Weigel, L. Bock, B. K. Gier, A. Lauer, M. Righi, M. Schlund, K. Adeniyi, B. Andela, E. Arnone, P. Berg, L.-P. Caron, I. Cionni, S. Corti, N. Drost, A. Hunter, L. Lledó, C. W. Mohr, A. Paçal, N. Pérez-Zanón, V. Predoi, M. Sandstad, J. Sillmann, A. Sterl, J. Vegas-Regidor, J. von Hardenberg, and V. Eyring,

- “Earth System Model Evaluation Tool (ESMValTool) v2.0 – diagnostics for extreme events, regional and impact evaluation, and analysis of Earth system models in CMIP,” *Geoscientific Model Development*, vol. 14, no. 6, pp. 3159–3184, 2021.
- [19] S. Rasp, H. Schulz, B. B. Stevens, and S. Bony, “Combining crowd-sourcing and deep learning to understand meso-scale organization of shallow convection,” in *AGU Fall Meeting 2019*, AGU, 2019.
- [20] V. Zantedeschi, F. Falasca, A. Douglas, R. Strange, M. Kusner, and D. Watson-Parris, “Cumulo: A dataset for learning cloud classes,” in *Proceedings of the NeurIPS 2019 Workshop Tackling Climate Change with Machine Learning*, Climate Change AI, 2019.
- [21] L. Denby, “Discovering the Importance of Mesoscale Cloud Organization Through Unsupervised Classification,” *Geophysical Research Letters*, vol. 47, no. 1, pp. 1–10, 2020.
- [22] T. Kurihana, E. Moyer, R. Willett, D. Gilton, and I. Foster, “Data-Driven Cloud Clustering via a Rotationally Invariant Autoencoder,” *IEEE Transactions on Geoscience and Remote Sensing*, pp. 1–25, 2021. arXiv: 2103.04885.
- [23] C. Zhang, X. Zhuge, and F. Yu, “Development of a high spatiotemporal resolution cloud-type classification approach using Himawari-8 and CloudSat,” *International Journal of Remote Sensing*, vol. 40, no. 16, pp. 6464–6481, 2019.
- [24] J. Lee, R. C. Weger, S. K. Sengupta, and R. M. Welch, “A Neural Network Approach to Cloud Classification,” *IEEE Transactions on Geoscience and Remote Sensing*, vol. 28, no. 5, pp. 846–855, 1990.
- [25] W. B. Rossow and R. A. Schiffer, “Advances in Understanding Clouds from ISCCP,” *Bulletin of the American Meteorological Society*, vol. 80, no. 11, pp. 2261–2287, 1999.
- [26] P. Kuma, F. A. Bender, A. Schuddeboom, A. J. Mcdonald, and Ø. Seland, “Machine learning of cloud types shows higher climate sensitivity is associated with lower cloud biases.[preprint],” *Atmos. Chem. Phys. Discuss. [preprint]*, no. March, 2022.
- [27] C. Jakob and G. Tselioudis, “Objective identification of cloud regimes in the Tropical Western Pacific,” *Geophysical Research Letters*, vol. 30, no. 21, pp. 1–4, 2003.
- [28] N. D. Gordon, J. R. Norris, C. P. Weaver, and S. A. Klein, “Cluster analysis of cloud regimes and characteristics dynamics of midlatitude synoptic systems in observations and a model,” *Journal of Geophysical Research D: Atmospheres*, vol. 110, no. 15, pp. 1–13, 2005.
- [29] R. Pincus, S. Platnick, S. A. Ackerman, R. S. Hemler, and R. J. Patrick Hofmann, “Reconciling simulated and observed views of clouds: MODIS, ISCCP, and the limits of instrument simulators,” *Journal of Climate*, vol. 25, no. 13, pp. 4699–4720, 2012.
- [30] L. Oreopoulos, N. Cho, D. Lee, and S. Kato, “Radiative effects of global MODIS cloud regimes,” *Journal of Geophysical Research: Atmospheres*, 2016.
- [31] J. Tan, C. Jakob, W. B. Rossow, and G. Tselioudis, “Increases in tropical rainfall driven by changes in frequency of organized deep convection,” *Nature*, vol. 519, no. 7544, pp. 451–454, 2015.
- [32] A. H. Young, K. R. Knapp, A. Inamdar, W. Hankins, and W. B. Rossow, “The international satellite cloud climatology project h-series climate data record product,” *Earth System Science Data*, vol. 10, no. 1, pp. 583–593, 2018.
- [33] G. Tselioudis, W. B. Rossow, C. Jakob, J. Remillard, D. Tropf, and Y. Zhang, “Evaluation of Clouds, Radiation, and Precipitation in CMIP6 Models Using Global Weather States Derived From Isccp-H Cloud Property Data,” *Journal of Climate*, pp. 1–42, 2021.
- [34] Z. Wang, “CloudSat 2B-CLDCLASS-LIDAR Product Process Description and Interface Control Document,” no. April, pp. 1–59, 2019.
- [35] S. Platnick, M. D. King, S. A. Ackerman, W. P. Menzel, B. A. Baum, J. C. Riédi, and R. A. Frey, “The MODIS cloud products: Algorithms and examples from terra,” *IEEE Transactions on Geoscience and Remote Sensing*, vol. 41, no. 2 PART 1, pp. 459–472, 2003.
- [36] M. Stengel, S. Stapelberg, O. Sus, C. Schlundt, C. Poulsen, G. Thomas, M. Christensen, C. C. Henken, R. Preusker, J. Fischer, A. Devasthale, U. Willén, K. G. Karlsson, G. R. McGarragh, S. Proud, A. C. Povey, R. G. Grainger, J. F. Meirink, A. Feofilov, R. Bennartz, J. S. Bojanowski, and R. Hollmann, “Cloud property datasets retrieved from AVHRR, MODIS, AATSR and MERIS in the framework of the Cloud-cci project,” *Earth System Science Data*, vol. 9, no. 2, pp. 881–904, 2017.
- [37] K. Sassen, Z. Wang, and D. Liu, “Global distribution of cirrus clouds from CloudSat/cloud-aerosol lidar and infrared pathfinder satellite observations (CALIPSO) measurements,” *Journal of Geophysical Research Atmospheres*, vol. 114, no. 8, pp. 1–12, 2008.
- [38] D. M. Winker, C. A. Hostetler, M. A. Vaughan, and A. H. Omar, “CALIOP Algorithm Theoretical Basis Document Part 1 : CALIOP Instrument, and Algorithms Overview,” *Release*, pp. 1–29, 2006.
- [39] M. Stengel, S. Stapelberg, O. Sus, S. Finkensieper, B. Würzler, D. Philipp, R. Hollmann, C. Poulsen, M. Christensen, and G. McGarragh, “Cloud_cci Advanced Very High Resolution Radiometer post meridiem (AVHRR-PM) dataset version 3: 35-year climatology of global cloud and radiation properties,” *Earth System Science Data*, vol. 12, no. 1, pp. 41–60, 2020.
- [40] O. Sus, M. Stengel, S. Stapelberg, G. McGarragh, C. Poulsen, A. C. Povey, C. Schlundt, G. Thomas, M. Christensen, S. Proud, M. Jerg, R. Grainger, and R. Hollmann, “The Community Cloud retrieval for CLimate (CC4CL) – Part 1: A framework applied to multiple satellite imaging sensors,” *Atmospheric Measurement Techniques*, vol. 11, no. 6, pp. 3373–3396, Jun. 2018.
- [41] J. Behrmann, W. Grathwohl, R. T. Chen, D. Duvenaud, and J. H. Jacobsen, “Invertible residual networks,” *36th International Conference on Machine Learning, ICML*

- 2019, vol. 2019-June, pp. 894–910, 2019. arXiv: 1811.00995.
- [42] L. Breiman, “Random Forests,” *Machine Learning*, no. 45, pp. 5–32, 2001.
 - [43] A. Walther, W. Straka, and A. K. Heidinger, “NOAA NESDIS Center for Satellite Applications and Research ABI Algorithm Theoretical Basis Document For Daytime Cloud Optical and Microphysical Properties (DCOMP),” no. June, pp. 1–66, 2013.
 - [44] Y. Lee, C. D. Kummerow, and I. Ebert-Uphoff, “Applying machine learning methods to detect convection using Geostationary Operational Environmental Satellite-16 (GOES-16) advanced baseline imager (ABI) data,” *Atmospheric Measurement Techniques*, vol. 14, no. 4, pp. 2699–2716, 2021.
 - [45] V. A. Gorooh, S. Kalia, P. Nguyen, K. lin Hsu, S. Sorooshian, S. Ganguly, and R. R. Nemani, “Deep Neural Network Cloud-Type Classification (DeepCTC) model and its application in evaluating PERSIANN-CCS,” *Remote Sensing*, vol. 12, no. 2, 2020.

Supporting information for the manuscript “Machine-learned cloud classes from satellite data for process-oriented climate model evaluation”

Arndt Kaps, Axel Lauer, Gustau Camps-Valls, *Fellow, IEEE*,
Pierre Gentine, Luis Gómez-Chova, *Senior Member, IEEE*,
Veronika Eyring

S1. OVERVIEW

In addition to the results presented in the main body of our paper, here we illustrate four more ways to evaluate our methods performance. We reinforce the validity of the results by showing that the predicted classes used in both our machine learning models are physically consistent with expectations. Furthermore, we investigate the importance of the different features used as inputs to our models with different metrics. We also compare results obtained by using different horizontal coarse graining resolutions as well as temporal resolutions.

S2. PHYSICAL CONSISTENCY

By analysing the features associated with each class we can show that the properties of the predicted classes are consistent with the expected properties from the meteorological definition of the respective cloud type (WMO Cloud Atlas). In Fig. S1, we show the distribution of the features for the two most common classes Ci and Sc. The values for each feature are normalized to the range $[0, 1]$, with zero and one corresponding to the minimum and maximum value observed across all classes. We find that the Ci class predicted by the IResNet has a higher cloud top and is exclusively flagged as ice. In addition, Ci clouds show a smaller water content and optical thickness. Similarly, we find that clouds are identified as Sc when a tile contains low-level clouds with a higher liquid than ice content and a higher optical thickness than Ci. Most other cloud classes also show consistent feature characteristics. The exception are the classes Sc and St, which the IResNet predicts for very similar ranges of the feature values. This is, however, in itself in line with the definitions of the cloud classes, as stratus and stratocumulus clouds have similar physical properties, leading to potential difficulties in the identification between the two classes.

The analysis of the physical consistency of the regression results is slightly more involved. As most grid boxes include several classes, we cannot simply show the feature values associated with individual cloud classes like we did for the classification. Instead, we analyze the characteristic feature values for grid cells predicted to have an especially high fraction of a specific class. As an example, Fig. S2 shows the feature value distribution for grid cells predicted to have a high fraction of Ci or Sc classes. This allows for a comparison between the properties of the classes obtained in the pixel-wise classification (Fig. S1) and the class fractions of the grid boxes (Fig. S2). Most prominent are the differences in liquid/ice particle radii between the two sets of grid cells. The respective values are consistent with cirrus being comprised of ice and stratocumulus consisting mostly of liquid particles.

These plots also show that grid cells with a high fraction of Sc typically have higher cloud top pressures (i.e. lower cloud top heights) and contain more condensed water than grid cells with a high fraction of Ci. As expected, we find that the predictions of the regression model for high fractions of a cloud class are based on a similar feature values as the predictions on the pixel level. This shows that the regression model can indeed predict cloud classes from average states of large grid cells distinctly and that the physical basis used for the CloudSat classification is propagated throughout the individual steps of our method.

We can perform similar analysis on the results obtained using the ESACCI data, also taking into account regional prevalence of certain features. Fig. S3 shows global maps of predictions for the Ci and Cu classes and the features *ceri* and *ptop*. We find a high Cu fraction particularly in the subtropical subsidence regions characterized by a high average cloud top pressure. These areas contain essentially no predicted Ci clouds. In contrast, Ci clouds are frequently predicted in low- and mid-latitude regions and are characterized by a large ice content, visible as the large mean values of $ceri > 15 \mu m$. This is consistent with the expectation that cirrus clouds are characterized by high cloud tops and high relative ice content, whereas the opposite applies to shallow cumulus. Indeed, the fraction of Ci is slightly positively correlated with *ceri* (Pearson correlation $c_P = 0.18$) and anti-correlated with *ptop* ($c_P = -0.56$), while the opposite is true for Cu (*ceri*: $c_P = -0.4$, *ptop*: $c_P = 0.29$). This is another indicator for the physical consistency of the predicted class fractions with the WMO cloud types.

S3. FEATURE IMPORTANCE

Beyond the physical relationship of the classes to the features, we can also determine which features are important for the model to provide good predictions. We did this for the regression model, because this will be the model that is applied on new datasets, where not all features might be available. Note that the following analysis applies only to this specific model. A model trained on fewer features might rely on a different combination of these.

First, we analysed the features of the regression model using the permutation importance method. This method quantifies the impact of shuffling individual features throughout the data while keeping all other features fixed. The importance is measured in terms of the decrease of chosen metrics, of which we use both the R2-score and the mean squared error (MSE). These metrics are displayed in Fig. S4 for an RF trained on $(100 \text{ km})^2$ grid cells. The permutation importance can both be computed on the train (Fig. S4b) and test data (Fig. S4a). A high importance in the train split can indicate that the model overfits on the respective feature. The importance in the test split highlights the features important for generalization. However, for our case the permutation importance is virtually identical for both splits, indicating good generalization to the test set. The features *tsurf* and *ptop* seem to have the largest impact on both the R2-Score and the MSE when permuted, followed by *ceri* and *cod*.

The permutation importance can be skewed when features are correlated, as information about the permuted feature can be

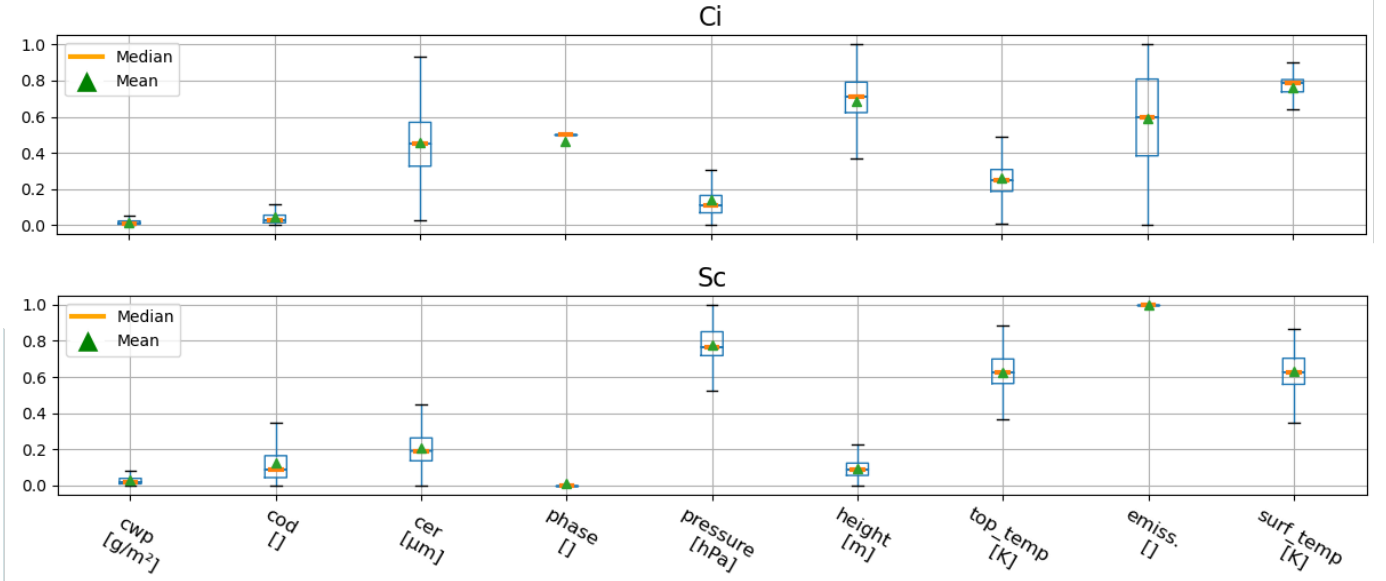


Fig. S1: Distributions of the feature values for IResNet predictions of the two most common classes in the CUMULO classification, Ci (top) and Sc (bottom). The values are min/max scaled such that the feature values for all classes lie in the same range. Phase is a categorical feature: 0 for liquid, 0.5 for ice and 1 for undetermined. Boxes extend from lower to upper quartile, and whiskers extend from 10th to 90th percentile. Comparing the relative locations of the boxes between the classes allows assessment of the physical properties the IResNet associates with the respective classes. For example, the cloud top pressure values for Ci are at the low end of the range, while the opposite is true for Sc.

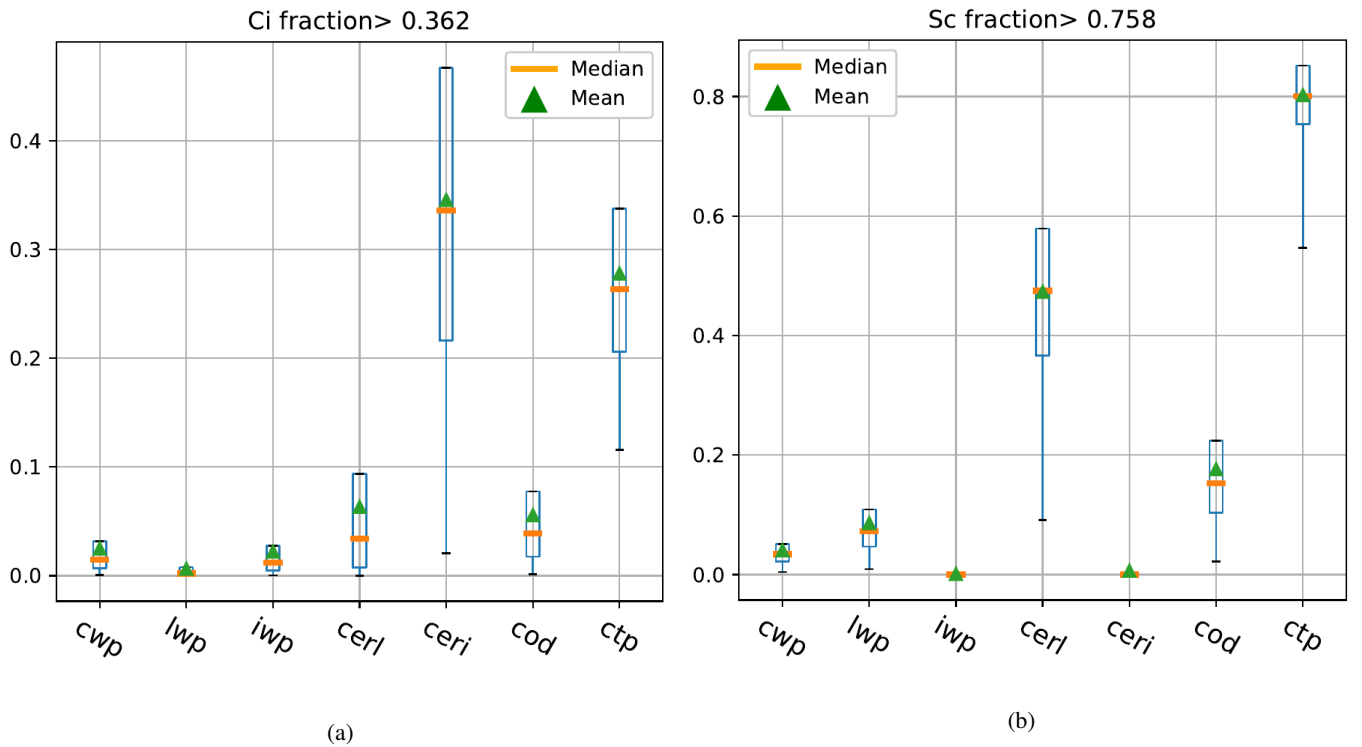


Fig. S2: Distribution of the feature values of grid cells predicted by the RF to have a large fraction of Ci (left) or Sc (right) (90% quantile, i.e. thresholds 0.362 for Ci and 0.758 for Sc; see also Fig. S1). The boxes indicate the ranges of the individual features which the RF associates with especially high occurrences of the respective class. Box ranges as in Fig. S1; values scaled such that 0 and 1 corresponds to the minimum and maximum values found across all classes, respectively.

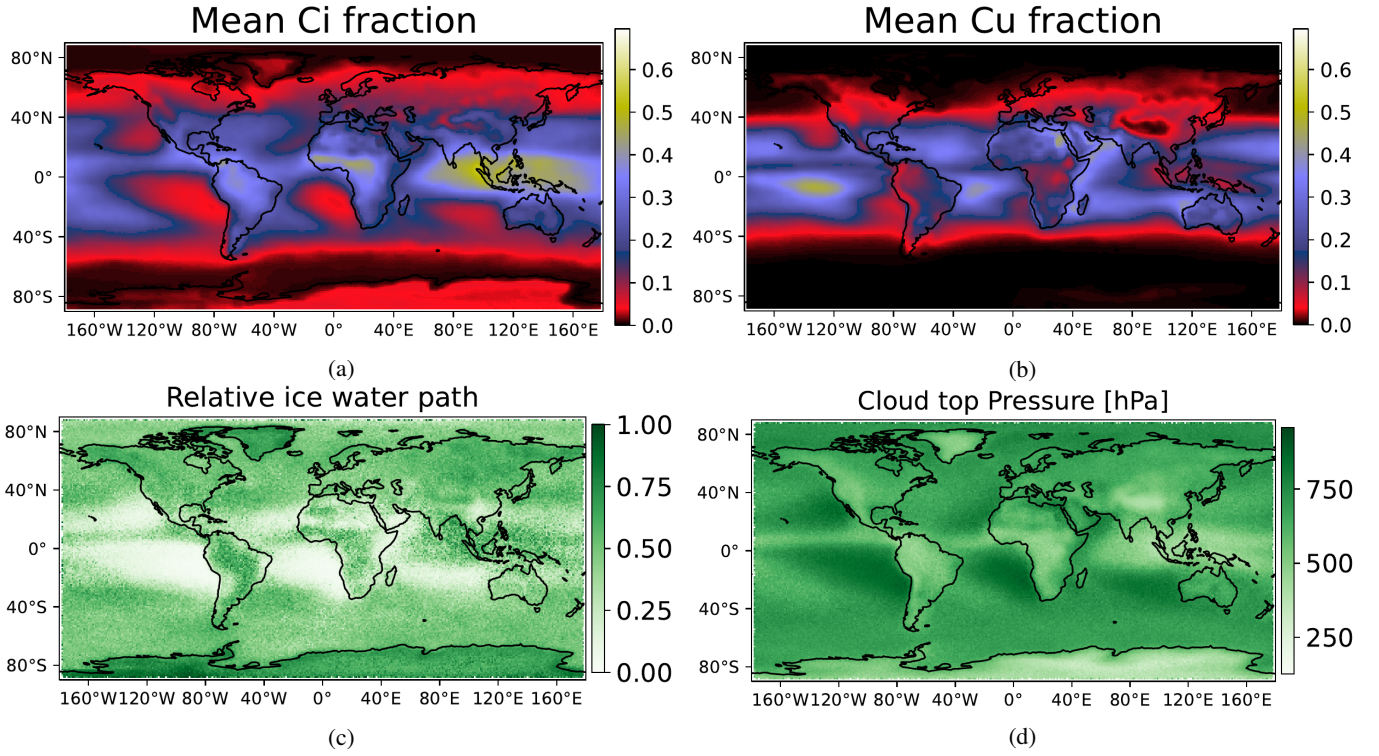


Fig. S3: Mean predicted class fractions for Ci(S3a) and Cu(S3b) compared to the mean feature values for $ptop$ (S3d) and the relative ice water path. Grid cells are 100×100 pixels and the RF was trained on $(100 \text{ km})^2$ grid cells using the optimal set of features.

inferred from its correlated values. As Fig. S4d shows, all features but $tsurf$ are strongly correlated with at least one other feature ($|c_P| \geq 0.69$). This might lead to a comparatively high feature importance for $tsurf$. However using correlated features has still proven to be useful to the results. Even though most of the features are correlated with at least one other feature, these correlated features provide additional information that would otherwise be lost when spatially averaged.

We additionally took into account the mean decrease in impurity (MDI) attributable to the individual features (Fig. S4c). The importances produced this way are similar to those indicated by the permutation importance using MSE.

Taken together, these feature importance measures indicate that the model relies strongly on $ptop$ for its predictions. The results for the other features are less clear but a strong dependence on $ceri$ and cod is likely, since their impact ranks high across all measures. Due to the correlated features and the fact that the MDI can only be determined for the test set these results however only give a rough indication about which features are required for successful application of our method to climate models. The high importance these measures attribute to $tsurf$ is however unexpected.

S4. IMPACT OF CHANGING THE COARSE GRAINING RESOLUTION OF ESACCI

The MODIS and ESACCI data can not be coarse grained such that corresponding grid cells everywhere on the globe cover the same area. This could be achieved by interpolative regridding, which we want to avoid here. We instead aim to find a coarse grained resolution that is most similar to

the other across the globe and assume that the grid cell averaging mitigates resulting differences. We have therefore evaluated the RF trained on a fixed grid cell size from coarse grained MODIS on different resolutions of the ESACCI data. We applied an RF trained on $(100 \text{ km})^2$ grid cells on $(0.5^\circ)^2$, $(2.5^\circ)^2$ and $(5^\circ)^2$ ESACCI grid cells. Fig. S5 compares these results using the most common cloud type, binned to a $1^\circ \times 1^\circ$ grid as well as the zonal average of the As class. Note that again, the cloud distributions per coarse grained grid cell are interpreted as point values for the grid cell center. The representation using the most common cloud type, while being useful to represent the result in a single plot, hides the less prevalent cloud types, such that only Sc (teal), Ci (gold), As (dark green), Ac (blue) and Cu (light green) are displayed. The results show, that the global class distributions stay similar, but some features shift depending on the resolution. The other cloud types do however not disappear completely in the predictions but are being “hidden” in this representation. For example, we see that the Cu class gets hidden by Ci when the resolution is decreased. An interesting difference is the increase in As fraction in central Asia with decreasing resolution. Furthermore, the zonal averages of Ac show that with decreasing resolution the variability of the predictions decreases as well. The zonal mean of Ac however stays the same for all three resolutions.

We conclude that if trained on data coarse grained to around $(100 \text{ km})^2$, the method can provide useful predictions on any resolution typical for ESMs. Even though, some classes with similar regional occurrence might “switch places”, the zonal distributions stay essentially the same across resolutions

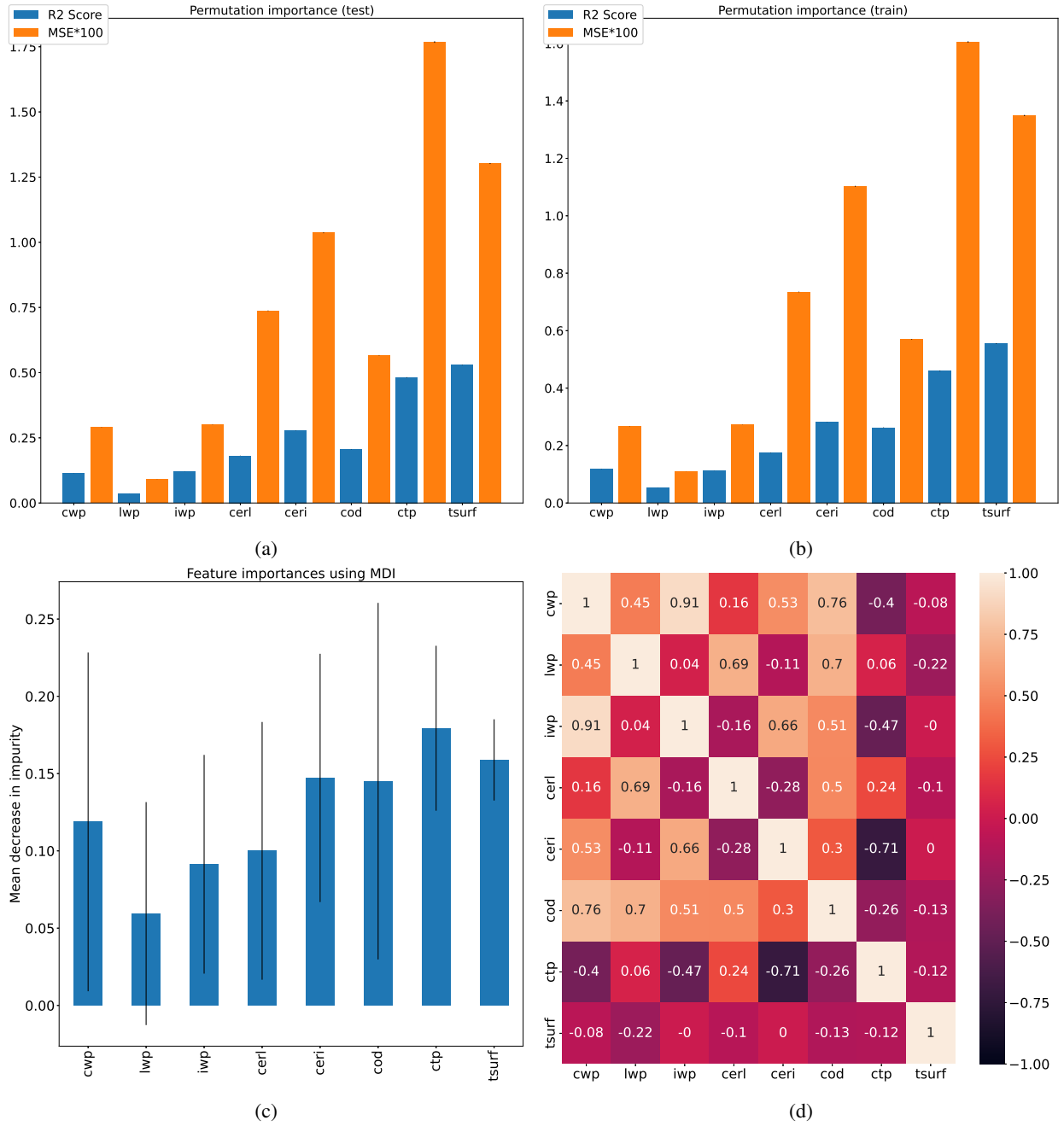


Fig. S4: Analysing the impact the individual features used in the regression have on the predictions of the RF. S4a: Permutation importance, in terms of the R2-Score and the mean squared error (scaled for visibility), computed on the test split of the data. Standard deviation is shown but so small it is barely visible. S4b: same as S4a but computed on the train split. In both cases the importance was computed for a dataset of one million samples, using 20 different permutations per feature. S4c: Mean decrease in impurity with standard deviation over all trees. S4d: Pearson correlation of the features .

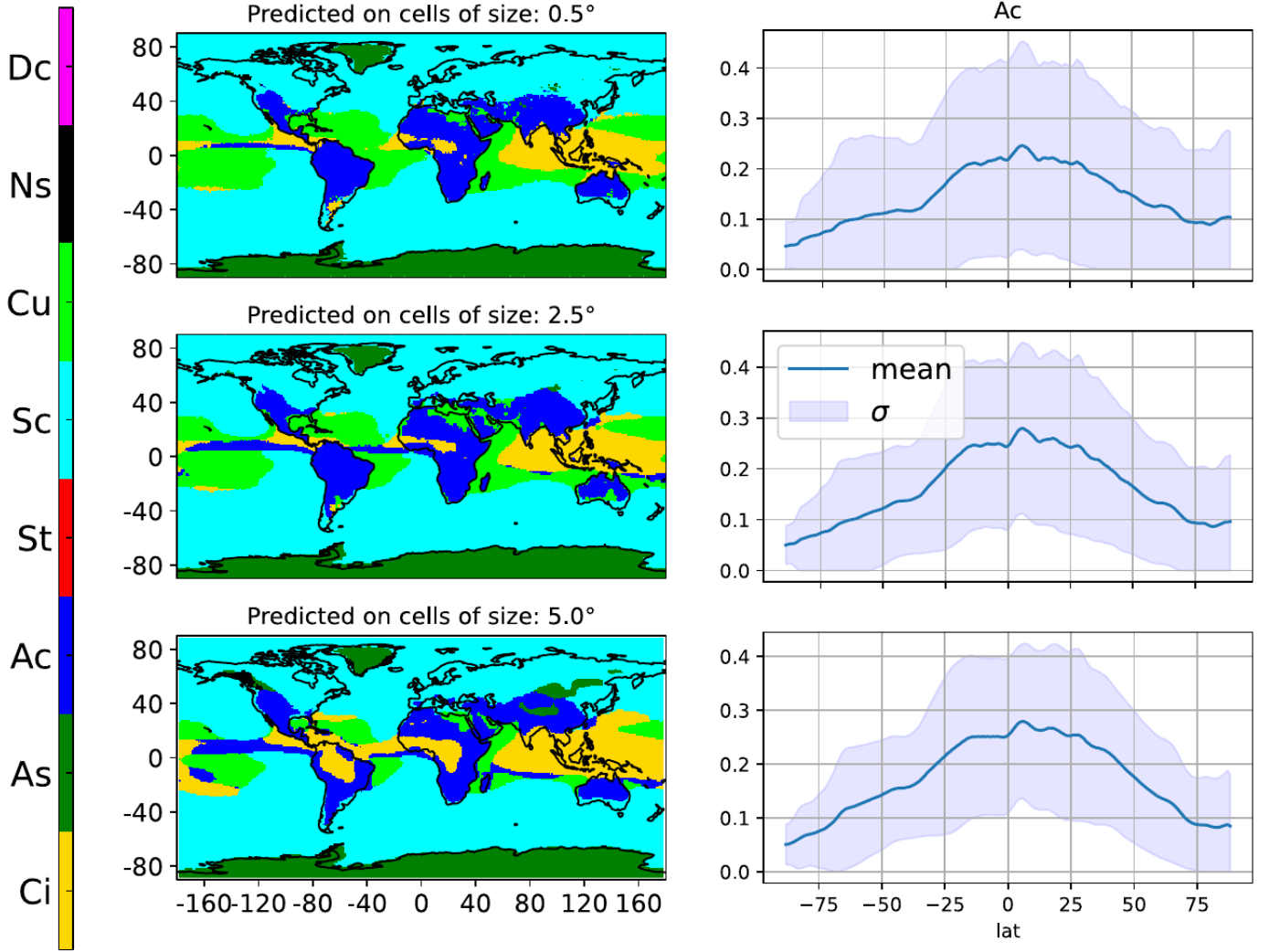


Fig. S5: Results for predictions performed on ESACCI data with different coarse graining resolutions. The panels on the left show the most common cloud type in each $1^\circ \times 1^\circ$ area, while those on the right show the zonal average for the Ac class.

indicating no fundamental changes.

S5. IMPACT OF TEMPORAL RESOLUTION

The results shown in the main paper were produced by training and applying the machine-learning models to instantaneous data. Climate models, however, often provide output in the form of daily or monthly averages. This averaging process might introduce deviations from the feature distributions obtained with instantaneous data. The impact of using temporally averaged data is investigated in the following using averaged inputs for the regression model. Here, we use the two daily measurements from the ascending and descending orbits provided by the ESACCI dataset. We compare the results to the ones obtained with the same regression model applied to instantaneous data. Exemplary results for using features from the instantaneous and mean input data are shown in Fig. S6 and Fig. S7, respectively. For all classes, the distributions look very similar, also to the results obtained using an RF trained and applied on higher resolution data (Fig. 6 in the main paper). The per class correlations range between $c_P^{Dc} = 0.714$ and

$c_P^{As} = 0.893$, with unweighted mean $\overline{c_P} = 0.839$, this giving an indication that using daily averages instead of instantaneous features for this method is possible.

We applied the RF model trained on $(100 \text{ km})^2$ grid cells to ESACCI monthly mean (L3C) data. Fig. S8 shows that the average predicted fractions are similar to those of the instantaneous input data (Figures S6, S7), but with less pronounced geographical features. As one would expect from using monthly means, the predicted fractions appear smoothed out and show rather similar magnitudes over large areas. The most notable difference in the representation of the individual classes with respect to using instantaneous data is the globally increased amount of the predicted Ns fraction. We see a further increase in Sc and a decrease in St compared to the distribution in CloudSat, suggesting that monthly mean data are not well suited as an input to our method. The increase in both Ns and As further suggests that the monthly average data show much larger effective ice particle radii than the instantaneous data. In fact we find a 4 fold increase in the median ice particle radius and similarly large increases in the cloud water path. Since

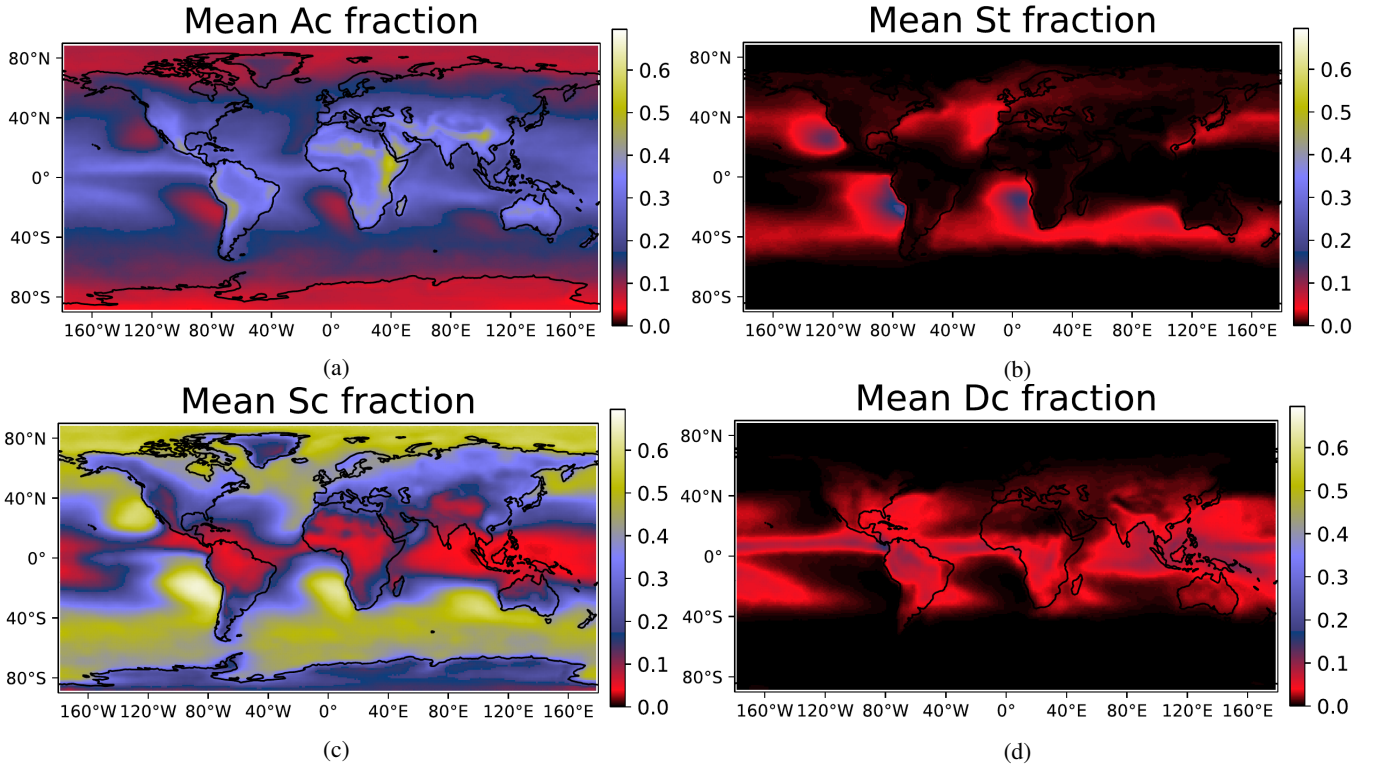


Fig. S6: Examples of predicted mean class fractions using feature values from instantaneous source data. Predictions were made using an RF trained on $(100 \text{ km})^2$ grid cells applied on 100×100 ESACCI pixels.

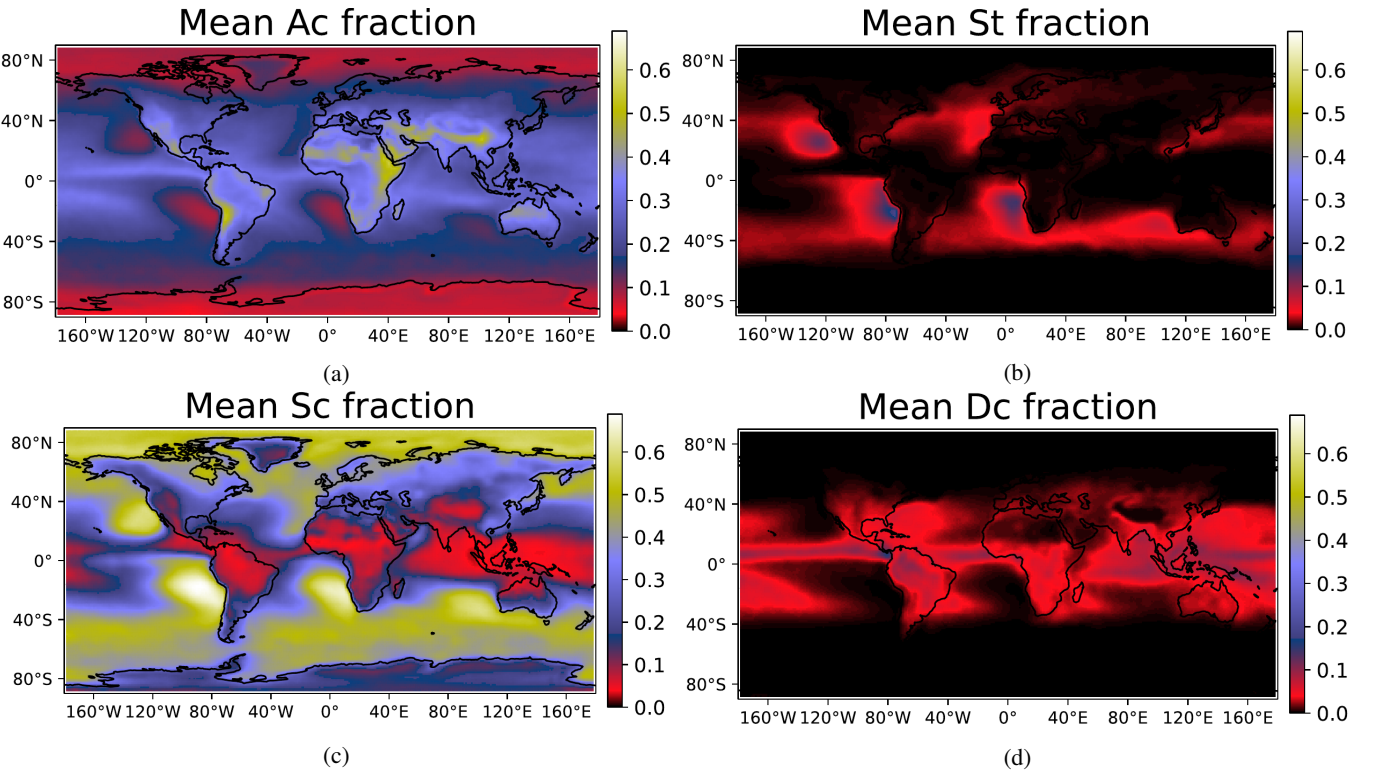


Fig. S7: Mean class fractions using feature values obtained by averaged over ascending and descending orbits. Predictions were made using the same RF as for Fig. S6, using 100×100 ESACCI pixels as well .

Mean cloud-type fractions

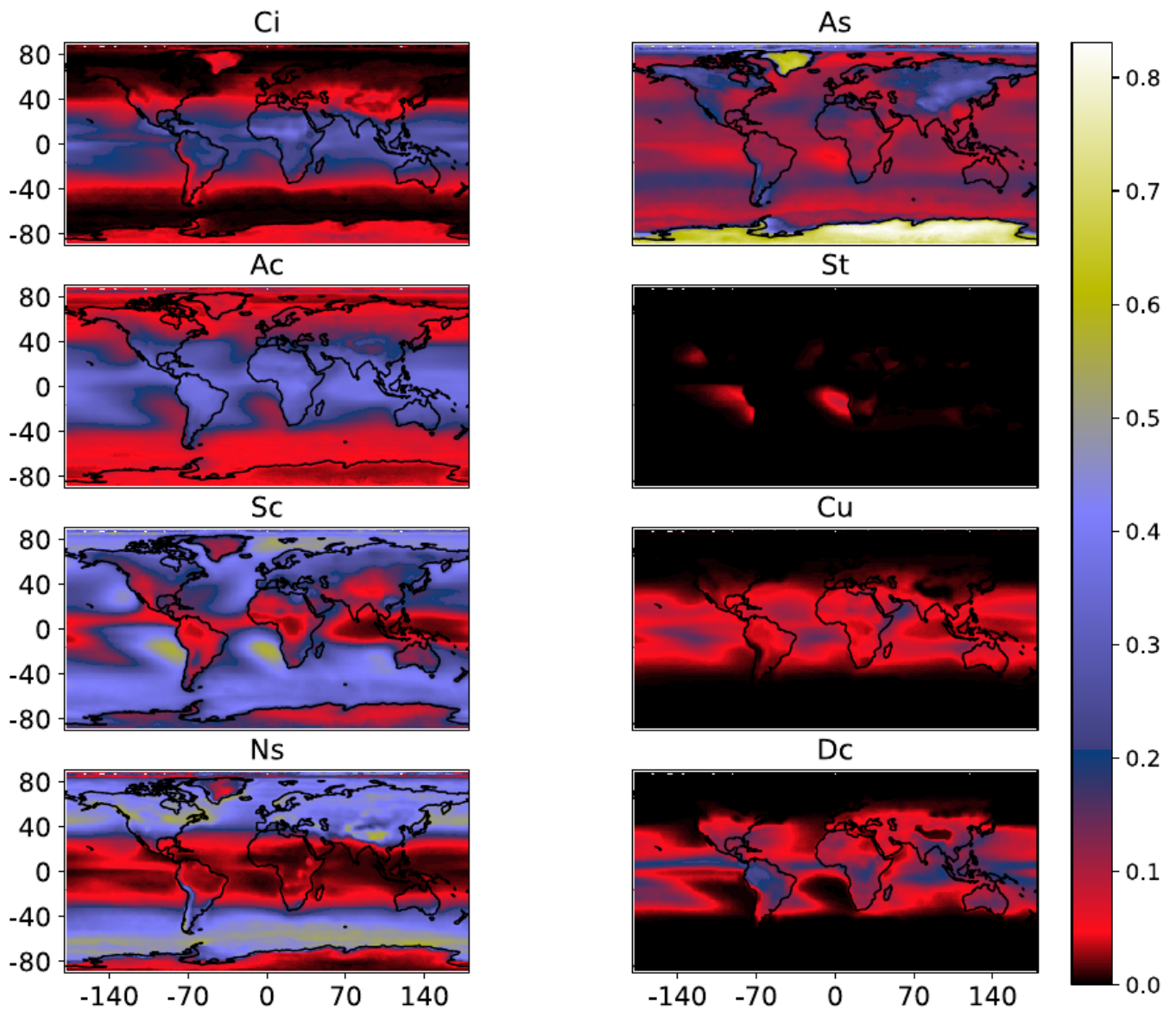


Fig. S8: Average predicted fractions using features obtained from monthly mean data (L3C), using the RF trained on $(100 \text{ km})^2$ grid cells. The source data consists of 220 months sampled randomly between 1984 and 2016. The grid cells are constructed from 10×10 ESACCI pixels of 0.5° resolution.

both, the L3C and L3U ESACCI data, are derived from the same instrument, the time averaging of the data must somehow cause this increase, which in turn causes the regression to produce unreliable results.